Engineering Geology 304 (2022) 106680

Contents lists available at ScienceDirect

Engineering Geology

journal homepage: www.elsevier.com/locate/enggeo

Large-scale landslide dam breach experiments: Overtopping and "overtopping and seepage" failures

Gordon G.D. Zhou [a,b,c], Shuai Li [a,b,d,*], Xueqiang Lu [a,b], Hui Tang [d]

[a] Key Laboratory of Mountain Hazards and Earth Surface Process/Institute of Mountain Hazards and Environment, Chinese Academy of Sciences (CAS), Chengdu, China
[b] University of Chinese Academy of Sciences, Beijing, China
[c] China-Pakistan Joint Research Center on Earth Sciences, CAS-HEC, Islamabad, Pakistan
[d] Section 4.7: Earth Surface Process Modelling, GFZ, Potsdam, Germany

ARTICLE INFO

Keywords:
Landslide dam
Large-scale experiments
Overtopping failure
"Overtopping and seepage" failure
Breach evolution
Channel morphology

ABSTRACT

Landslide dams form when landslide materials reach rivers causing complete or partial blockage. It is known that overtopping water flows and seepage flows are two crucial processes that induce dam failure. In several instances, the landslide dams collapse is caused by the coupled influence of seepage flows and overtopping water. This study aims to evaluate the contribution of seepage flows to the overtopping failure of landslide dams in terms of dam stability, breach duration, and flow discharge. We conducted two field experiment tests to simulate landslide dam failure modes: overtopping failure and overtopping-seepage coupling. Results show that the internal erosion due to seepage induces the loss of fine particles, resulting in a fourfold increase in dam deformation relative to when seepage is minimal. In the case overtopping and seepage failure, the outburst duration is shortened by two-thirds, but the peak outburst discharge is increased by nearly two times compared with the pure overtopping failure. Sediments accumulate at the downstream channel for overtopping failure, but erosion is observed before accumulation when the "overtopping and seepage" failure occurs. Fine grain sizes are limited to the downstream bed for both failure modes, which indicates the equal mobility of sediments involved in the outburst flood from a landslide dam breach.

1. Introduction

Landslide dams often form when landslide debris entirely or partially blocks rivers (Ermini and Casagli, 2003). The suddenness and unpredictability of landslide dam failures make them extremely destructive, posing a threat to human lives and the environment (Walder and O'Connor, 1997; Chai et al., 2000; Zhu and Li, 2001; Shang et al., 2003; Dai et al., 2005; Liu et al., 2010; Bonnard, 2011; Yan et al., 2020a; Yan et al., 2020b). The catastrophic M_S 8.0 Wenchuan earthquake triggered enormous landslides and landslide dams (Cui et al., 2011; Xu et al., 2009). Some of these dams subsequently breached and developed into outburst floods that devastated downstream communities' lives and infrastructure (Yin et al., 2009; Peng and Zhang, 2013; Fan et al., 2019). In addition, the erosion and deposition that result from dam outburst-induced floods lead to downstream channel instability and influence riverbed morphology (e.g., sandbars, armoring layers) (Korup, 2002; Liu et al., 2010; Chen et al., 2015; Jiang and Wei, 2020). It is, therefore, necessary to carry out quantitative studies on the causes of landslide dam failure and the impact of outburst floods on channel morphology to improve landslide dam hazard mitigation and disaster preparedness.

The failure modes of landslide dams can be divided into three categories (Fig. 1a, b, and c): overtopping failure, seepage failure, and "overtopping and seepage" failure (Schuster and Costa, 1986; Zhu et al., 2019). Overtopping failure occurs in landslide dams with low permeability, high soil strength of dam materials, and large upstream flow discharge. Seepage failure occurs when landslide dams are highly permeable and have low upstream flow discharge (Chen et al., 2015). The "overtopping and seepage" failure mainly occurs when dams have high permeability, are composed of weak dam materials, and have a considerable upstream flow discharge (Peng et al., 2016). The "overtopping and seepage" failure involves seepage flow on the downstream dam surface followed by subsequent overtopping erosion. Due to the narrow valleys and small impounding reservoirs in high mountain areas, the upstream water level rapidly increases once the landslide dam is

* Corresponding author at: Key Laboratory of Mountain Hazards and Earth Surface Process/Institute of Mountain Hazards and Environment, Chinese Academy of Sciences (CAS), Chengdu, China.
E-mail addresses: gordon@imde.ac.cn (G.G.D. Zhou), lishuai@imde.ac.cn (S. Li), luxueqiang18@mails.ucas.ac.cn (X. Lu), htang@gfz-potsdam.de (H. Tang).

https://doi.org/10.1016/j.enggeo.2022.106680
Received 14 July 2021; Received in revised form 17 April 2022; Accepted 22 April 2022
Available online 28 April 2022

formed. In such cases, seepage is minimized and the landslide dams are assumed to fail solely due to overtopping (Schuster and Costa, 1986; Peng et al., 2016). However, seepage in landslide dams is inevitable due to their poorly-sorted, unconsolidated, and heterogeneous material composition (Liao and Chou, 2003; Okeke and Wang, 2016). Thus, the "overtopping and seepage" failure mode often occurs in reality.

Although most landslide dams fail due to overtopping (Xu et al., 2009; Peng and Zhang, 2012; Peng et al., 2016), cases with seepage as the dominant failure mechanism have also been reported (Peng et al., 2014). Seepage induces internal erosion, which deforms the dam (Costa and Schuster, 1988; Peng et al., 2014). According to the tests of Liao and Chou (2003), seepage flow is one of the key factors that affect the stability of landslide dams and the outburst of flood discharge. Okeke and Wang (2016) found that the critical seepage flow rate increases with the dam crest width, dam height, and upstream inflow rate. Zhang et al. (2019) also reported that seepage and internal erosion could weaken the shear strength and increase the permeability of soils.

Several small-scale laboratory experiments have focused on the failure of landslide dams (Awal et al., 2008; Chen et al., 2015; Jiang and Wei, 2020; Xiangang et al., 2018; Zhou et al., 2019a; Zhu et al., 2019, 2020). However, few studies attempted to analyze the difference between overtopping and "overtopping and seepage" failures. The mechanism of dam failure due to the coupled effects of internal (seepage flow) and surface (overtopping) erosion is a critical question that can be explored through hydrodynamic perspectives using large-scale field tests.

In this study, we performed two large-scale landslide-dam experiments, one where overtopping is the only dominant failure mechanism; and another where both overtopping and seepage are relevant. The comprehensive investigation conducted here aims to (i) document dam settlement deformation before failure; (ii) directly measure the evolution of dam breach over time; (iii) investigate the difference of the outburst flood hydrographs; and (iv) assess the geomorphological changes in downstream channel caused by outburst floods.

2. Large-scale physical modeling tests

2.1. Model design

Scaling laws are crucial in designing physical modeling experiments. The potential energy of water, which influences the dam stability, failure mechanisms, and outburst floods, is related to the volume of the dammed lake (V_L), the dam height (H_d), and dam volume (V_d) (Costa and Schuster, 1988; Korup, 2002). The dam height (H_d) represents the water head of the dammed lake that triggers seepage flow, while the volume of the landslide dam (V_d) determines the mass of erodible soils during the failure process. The landslide dam toe to toe length (L_b) represents the potential seepage length. A set of dimensionless numbers, H_d / L_b, $V_d^{1/3} / H_d$, and $V_L^{1/3} / H_d$, were proposed to define the geometrical features of the landslide dam and dammed lake (Xu and Zhang, 2009; Peng and Zhang, 2012; Zhou et al., 2019a). These parameters are helpful to analyze the dam geometry and its potential failure modes. For example, the dam shape coefficient, $V_d^{1/3} / H_d$, reflects the erodible granular material available during dam breaching. The lake shape coefficient, $V_L^{1/3} / H_d$, indicates the potential volume of water that can erode the dam and influence the breach scale and the outflow discharge.

Fig. 2 shows data from more than 80 landslide dam cases worldwide, collected from the literature with dimensionless quantities (Zhou et al.,

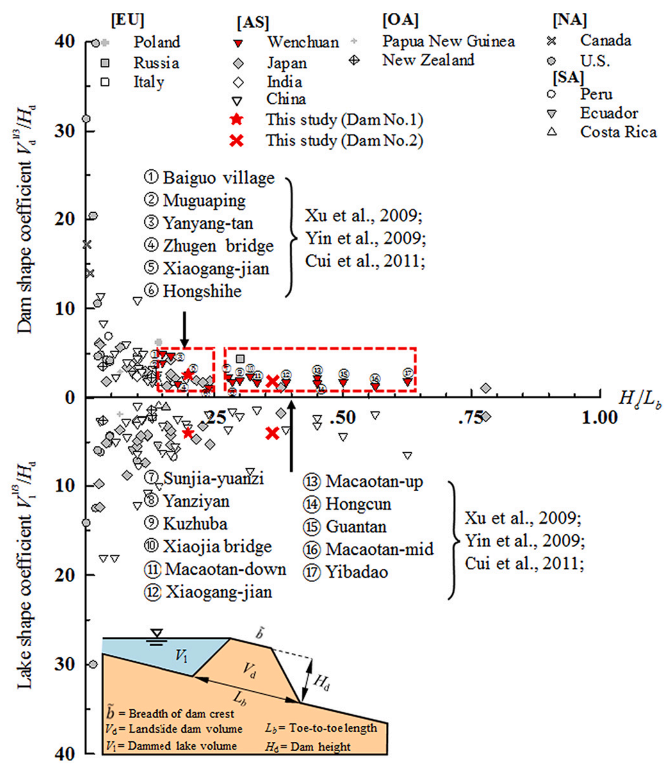

Fig. 2. Dimensionless parameters characterizing the geometry of landslide dams for cases derived from different datasets (Costa and Schuster, 1988; Korup, 2002; Xu et al., 2009; Yin et al., 2009; Peng and Zhang, 2012; Cui et al., 2011) ([EU] is Europe, [AS] is Asia, [OA] is Australia, [SA] is South America, and [NA] is North America).

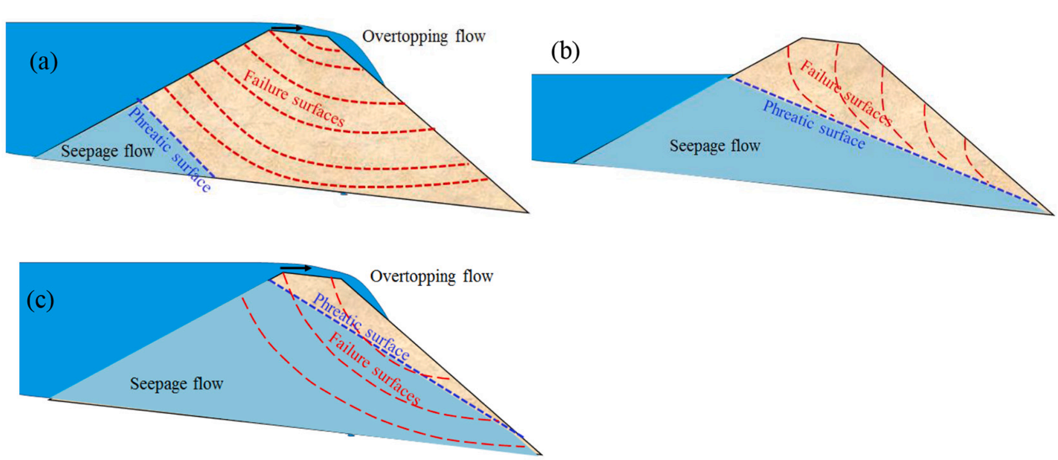

Fig. 1. Typical failure models of landslide dams; (a) overtopping failure model. (b) seepage failure model. (c) overtopping and seepage failure model.

2019a). Seventeen of these cases are induced by the Wenchuan M_S 8.0 earthquake (filled triangles in Fig. 2). The dimensionless coefficients that define the modeled dams in this study (red star and cross) fall within the range of values measured for natural landslide dams and can therefore be considered to represent realistic cases (Zhou et al., 2019a; 2019b). Fig. 2 shows that as H_d / L_b is increased, dams gradually transform from being broad and thick to being narrow and thin. Furthermore, we found that the landslide dams with low H_d / L_b (enclosed in a red dashed box on the left) mainly fail due to overtopping. In contrast, those with large H_d / L_b (circled in a red dashed box on the right) fail due to seepage/piping failure (Costa and Schuster, 1988; Korup, 2002; Xu et al., 2009; Yin et al., 2009; Peng and Zhang, 2012; Cui et al., 2011). Accordingly, one value of H_d / L_b in each group is considered in this study to investigate these two failure mechanisms. Namely, dam No.1 with H_d / L_b = 0.2 is a broad and thick dam, whereas dam No.2 with H_d / L_b = 0.36 is a narrow and thin dam. These two landslide dams are shown in Fig. 3. The height and transverse width of both dams are H_d = 2.0 m and 8.0 m, respectively. The top and bottom streamwise lengths L_b for Dam No. 1 are 5.0 m and 10.0 m, while they are 0.5 m and 5.5 m for Dam No. 2. The inclination angles of the upstream and downstream dam faces are $\alpha_1 = 38^\circ$ and $\alpha_2 = 39^\circ$, respectively, which are close to the natural repose angle of soils. The bottom slope of the dams is $\theta = 3^\circ$. The volume of the upstream reservoir is about 500 m^3 for both dams. Dam breaching was initiated by cutting a notch (width w_0: 0.5 m, depth h_0: 0.2 m) at the center of the dam crest.

Model dams are built according to the construction procedures adopted by dam-breach tests conducted by the EU IMPACT project (Morrism, 2008), U.S. Department of Agriculture (Hanson et al., 2005), Nanjing Hydraulic Research Institute, China (Zhang et al., 2009), and National Chung Hsing University (Feng et al., 2020). Real debris flow deposits from the Jiangjia Ravine (with an averaged inclined slope of θ = 3°), near the national Dongchuan Debris Flow Observation and Research Station (DDFORS), are used to construct the model dams (see Fig. 4). Dam materials are dumped from a fixed and equal height to ensure the similarity between the constructed models. After the dams are constructed, the void ratio (e = 0.72) and bulk density (ρ_d= 1570 kg/m^3) at different locations are measured. The measured void ratio falls within the range (e = 0.59 – 1.11) obtained by Chang and Zhang (2013a) for natural landslide dams. Meanwhile, we cleared out loose materials that remained on the dam's surface without compacting them. Finally, white 0.5 m × 0.5 m grids are drawn on the dam crest and downstream surface to aid in quantifying the deformation of the dam. The water from the Jiangjia Ravine is guided into the reservoir through a channel (Fig. 4). The inflow discharge was kept constant at ~0.1 m^3/s by a sharp-crested triangular weir installed upstream. The water rose to the notch level (H = 1.8 m) after ~5400 s. The breaching flood is guided to the downstream channel by levees of piled sandbags on the left bank and a concrete wall on the right.

2.2. Experimental instrumentation

The dam breaching process is recorded using two digital cameras (Nikon D610 digital single-lens-reflex) and two video cameras (SONY 150 FDR-AX40, 1440 × 1080 pixels, 25 fps) (see Fig. 4). Two cameras are located 3 m overhead and 10 m downstream of the landslide dam. Digital camera No. 1 records the dam breach processes and monitors the stream-wise (x-direction) dam deformation. Digital camera No. 2 monitors the depth-wise and lateral dam deformation and provides the series of photos used for Particle Image Velocimetry (PIV) analysis. The system of cameras allows us to do a three-dimensional survey of the dam deformation before and during failure. Two water level gauges are installed at the right bank of the reservoir and downstream channel to measure the flow depth. Video camera No. 3 on the right bank of the channel provides detailed oblique views of the dam breaching and subsequent outburst flow depth at the downstream channel. Video camera No. 4 on the left bank records the water levels in the reservoir. All the cameras are wireless and are connected to a remote-control switch that activates all camera shutters simultaneously.

A laser scanner (FARO_3D M70) is used to measure the topography downstream of the landslide dam before and after failures. The sensor records a single scan in an entire field of view with a resolution of ±2 mm. Images are post-processed using the FARO SCENE software, a comprehensive 3D point cloud processing and management tool that can handle high-resolution three-dimensional laser scans. We collected the digital orthophotos and densely populated triangular irregular network (TIN) digital terrain models (~100,000 3D points) for the reservoir, dam, and downstream channel. In addition, an uncrewed aerial vehicle (UAV) is used to record a bird's-eye view of the experiment.

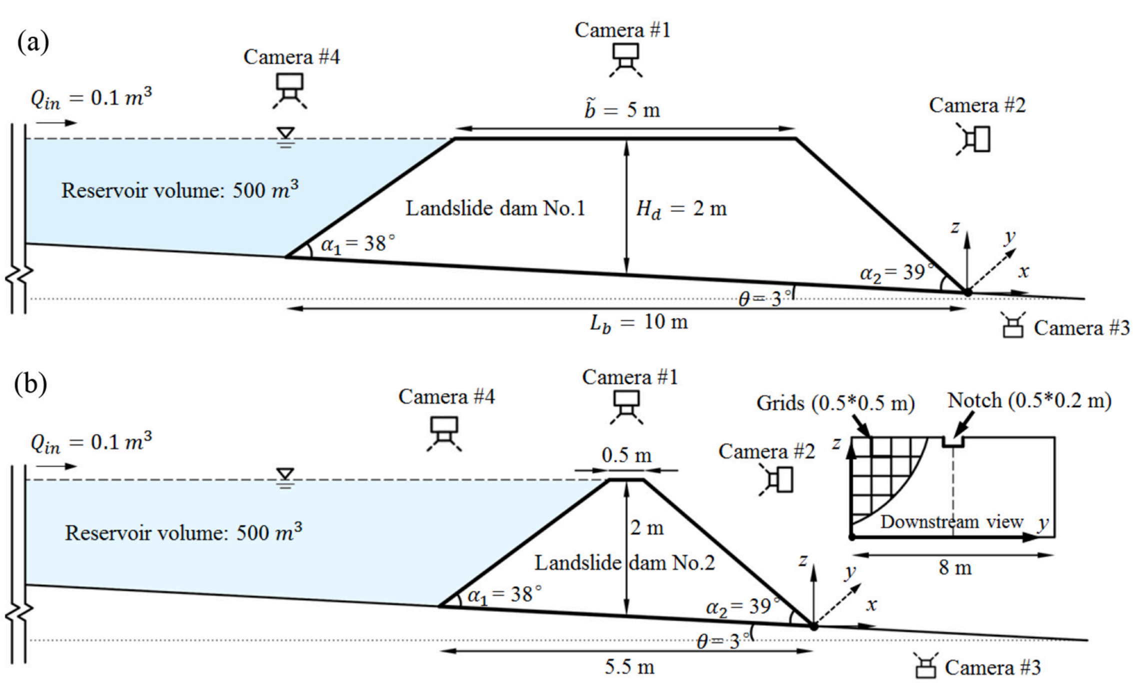

Fig. 3. Dimensions of (a) dam No. 1 and (b) dam No. 2 and their respective reservoirs used in the experiment.

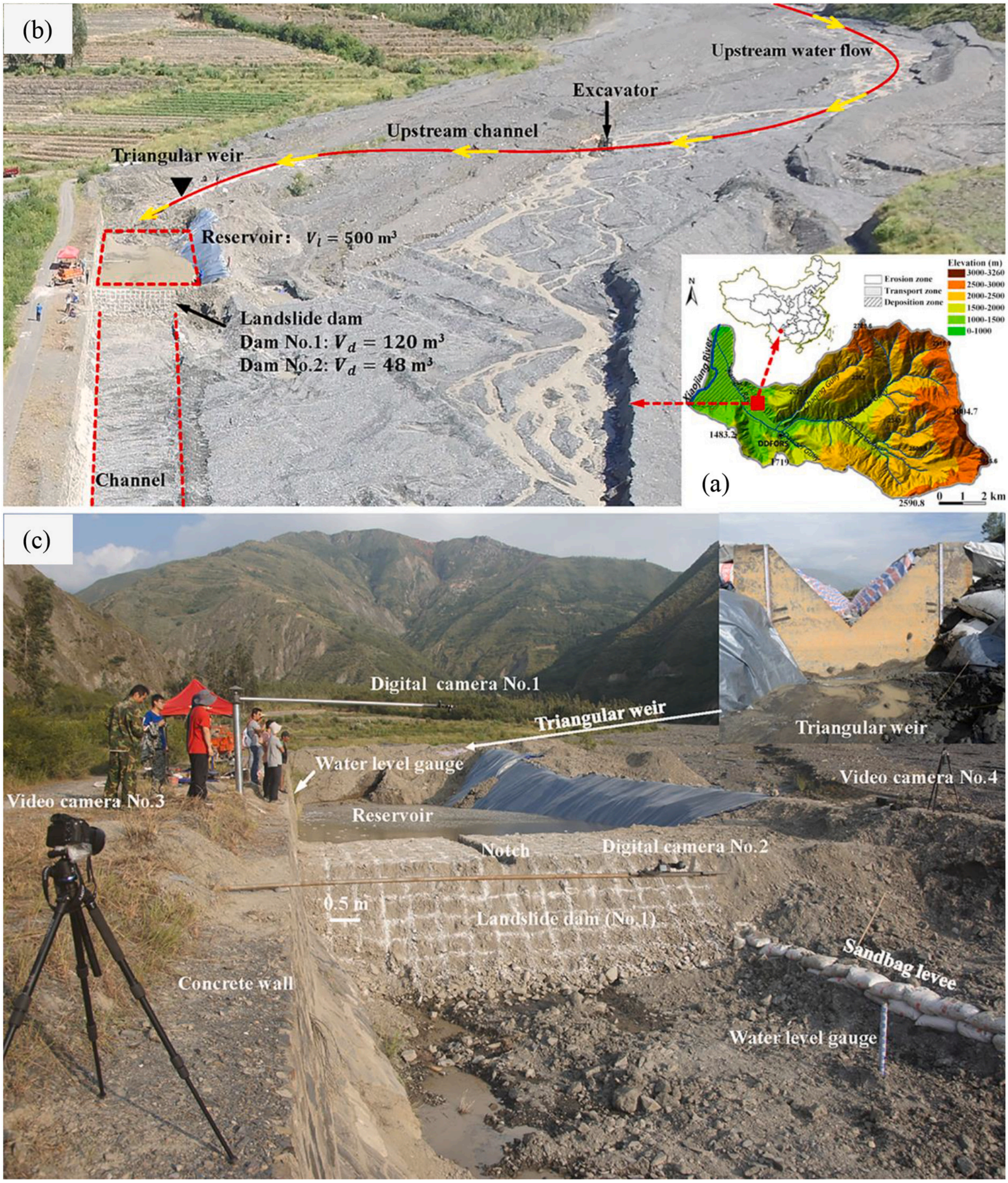

Fig. 4. (a) Location of the test site on the debris flow deposit fan of the Jiangjia Ravine. (b) A schematic diagram of the experimental setup, and (c) photographs of the instrumentation and equipment.

2.3. Granular materials

Natural landslide dams are usually composed of grains of various sizes from clay, sand, and gravel to cobbles and boulders (Costa and Schuster, 1988; Korup, 2002). The sediments from the debris flow fan of the Jiangjia Ravine have a moisture content of 6 ± 0.5% and are used to ensure that the experimental dams have a wide grain-size distribution. Grains are sifted through nine sieves with grid sizes between 0.25 mm and 60 mm. The fine particles that pass through a 0.25 mm sieve are measured using a Malvern Mastersizer 2000 instrument. The coarsest particles that could not pass through the largest sieve (60 mm) are approximately 300 mm in diameter. The grain size distribution (GSD) illustrated in Table 1 and Fig. 5 show that the channel-bed materials have a median grain size of $d_{50} = 12.4$ mm, a uniformity coefficient of $C_u = 22.44 > 5.0$, and a curvature coefficient of $1.0 < C_c = 1.16 < 3.0$. Referring to the particle diameter distribution standard, a good gradation is obtained when $C_u > 3$ and $C_c = 1{\sim}3$. These metrics suggest that the materials have poor sorting, wide gradation, and a bimodal distribution. Moreover, the GSD of dam materials in the experiment falls within the range of values that characterize natural landslide dams (shaded region in Fig. 5a).

Since the GSD of the materials that make up landslide dams control

Table 1
Soil properties of the modeled landslide dams.

Property	Value
d_{10}, d_{16}, d_{30}, d_{50}, d_{60}, d_{84}	0.90 mm, 2.20 mm, 4.60 mm, 12.40 mm, 20.2 mm, 79.80 mm
[a]$\sigma_g = d_{84}/d_{16}$, a dimensionless parameter for the spread in the grain size distribution	36.27
[b]$C_u = d_{60}/d_{10}$, uniformity coefficient	22.44
[b]$C_c = d_{30}^2/(d_{60} \times d_{10})$, curvature coefficient	1.16
[c]ρ_d, bulk density	1570 kg/m^3
e, void ratio	0.72
[c]φ, static friction angle of dry sediments	30°

[a] A dimensionless measure for the spread in the grain size distribution, cf. Walder, 2016

[b] SL237-1999, Geotechnical Test Procedure.

[c] Characteristic parameter of sediments at DDFORS, cf. Zhou and Ng, 2010

their stability and overall strength, as well as characterize the permeability of the dam material, they influence the erosional processes that can lead to failures by overtopping or seepage (Casagli et al., 2003). The bimodality index for GSD from Wilcock (1993) is calculated to quantify the bimodality in the sediment mixture:

$$B^* = \left(d_c/d_f\right)^{0.5}\left(F_c + F_f\right) \tag{1}$$

where d_c and d_f are the grain sizes of the coarse and fine parts, respectively. F_c and F_f are the proportions of sediment having sizes that fall under the primary (greater) amplitude and the secondary (lesser) amplitude, respectively. For the materials used in our model dams, these values are $d_f = 0.5$ mm, $d_c = 40$ mm, $F_c = 14.3\%$, and $F_f = 4.0\%$, from which $B^* = 1.64$ is obtained. This value is less than that obtained by Wilcock (1993), indicating that the sediment used in this study is weakly bimodal. To further characterize the modality of the dam materials, the standard deviation of sediment sizes is measured to characterize the variation of grain sizes downstream (Folk and Ward, 1957):

$$\sigma_\phi = [(\phi_{84} - \phi_{16})/4] + [(\phi_{95} - \phi_5)/6.6] \tag{2}$$

where σ_ϕ is the sorting index of the material, and $\phi_{84,16,95,5}$ are the respective percentile fractions of the bed material on the ϕ-scale ($\phi = \log_2 d$). The sorting index of the material in this study is $2 < \sigma_\phi = 2.21 < 4$, which indicates very poor sorting of sand and gravel, consistent with what is observed through visual inspection.

The soil-water characteristic curve (SWCC) and saturated permeability are two input parameters for seepage analysis based on Darcy's law of unsaturated soils (Ng and Pang, 2000). This study measures the SWCC of dam materials with diameters smaller than 2 mm through pressure plate tests. Permeability tests are carried out using a commercial flexible-wall permeameter through the falling head method. More details about the test apparatus and method can be found in ASTM D5084 (2010).

As shown in Fig. 6, the volumetric water content decreases as matric suction increases from 0.1 to 400 kPa for different soil samples. Specimens with high dry bulk density retain high volumetric water content for constant matric suction. This is consistent with previous studies reporting that dense soils have high water retention capacity (Ng and Pang, 2000; Mu et al., 2020). Note that soil specimens that pass through a 2 mm aperture sieve, from which the SWCC are measured, are finer

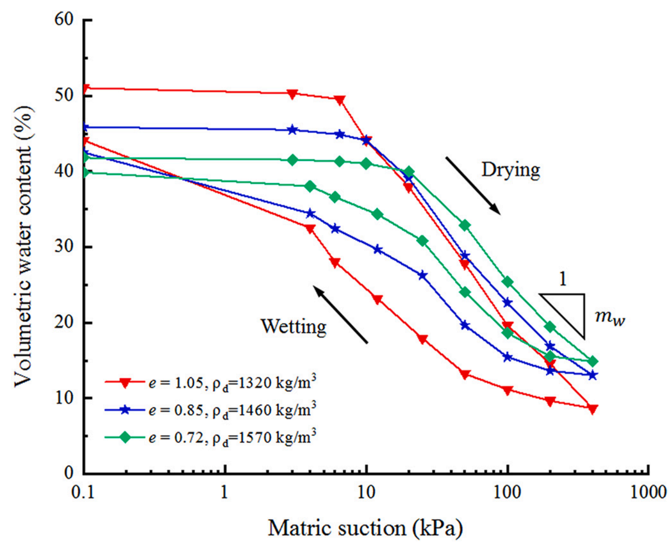

Fig. 6. Soil water characteristic curves of the sediment materials.

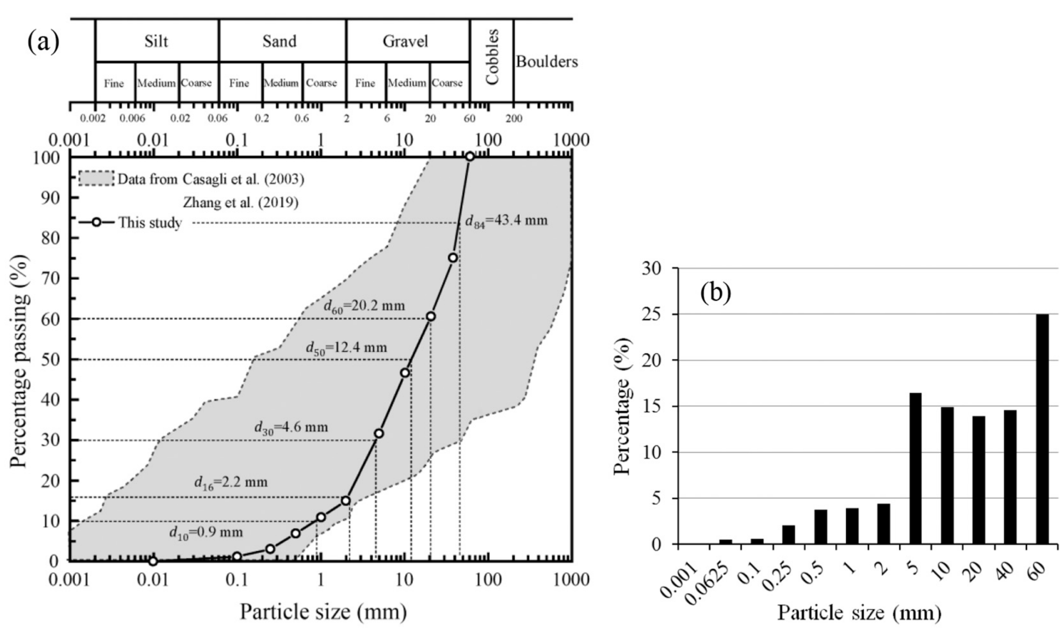

Fig. 5. The (a) grain size distribution (GSD) of granular materials used to construct the dams. The shaded region corresponds to the GSD range of 42 natural landslide dams in the Northern Apennines (cf. Casagli et al., 2003) while the dot-dashed line represents those obtained from this study. (b) The content of each grain size.

than the dam material from the field experiments.

3. Results

3.1. Landslide dam deformation before breaching

The unconsolidated dam body experiences uneven settlement during the impoundment of water in the reservoir. We chose the time over which the water fills the reservoir ($t = -5400$ s, see Figs. 7a and 8a for dams No. 1 and No. 2, respectively) and the start time of dam breach ($t = 0$ s, see Figs. 7b and 8b for dams No. 1 and No. 2, respectively) to analyze the deformation of two dams. Dam No. 1 slightly decreases with a maximum vertical settlement displacement of about 0.10 m relative to the original dam height (Fig. 7b). In comparison, a considerable vertical displacement of 0.40 m (four times larger than Dam No. 1) is observed for Dam No. 2 (Fig. 8b). The deformation of the landslide dams is quantified using Particle Image Velocimetry (PIV) technology, which relies on the cross-correlation between sequential images obtained by digital camera No. 2 to determine the average displacement within a limited area (White et al., 2003). PIV results show that the maximum settlement is 0.084 m and 0.379 m for Dam No. 1 and Dam No. 2, respectively as indicated by the arrow lengths in Fig. 7c and Fig. 8c. The results are consistent with the vertical displacement estimates of the dam height.

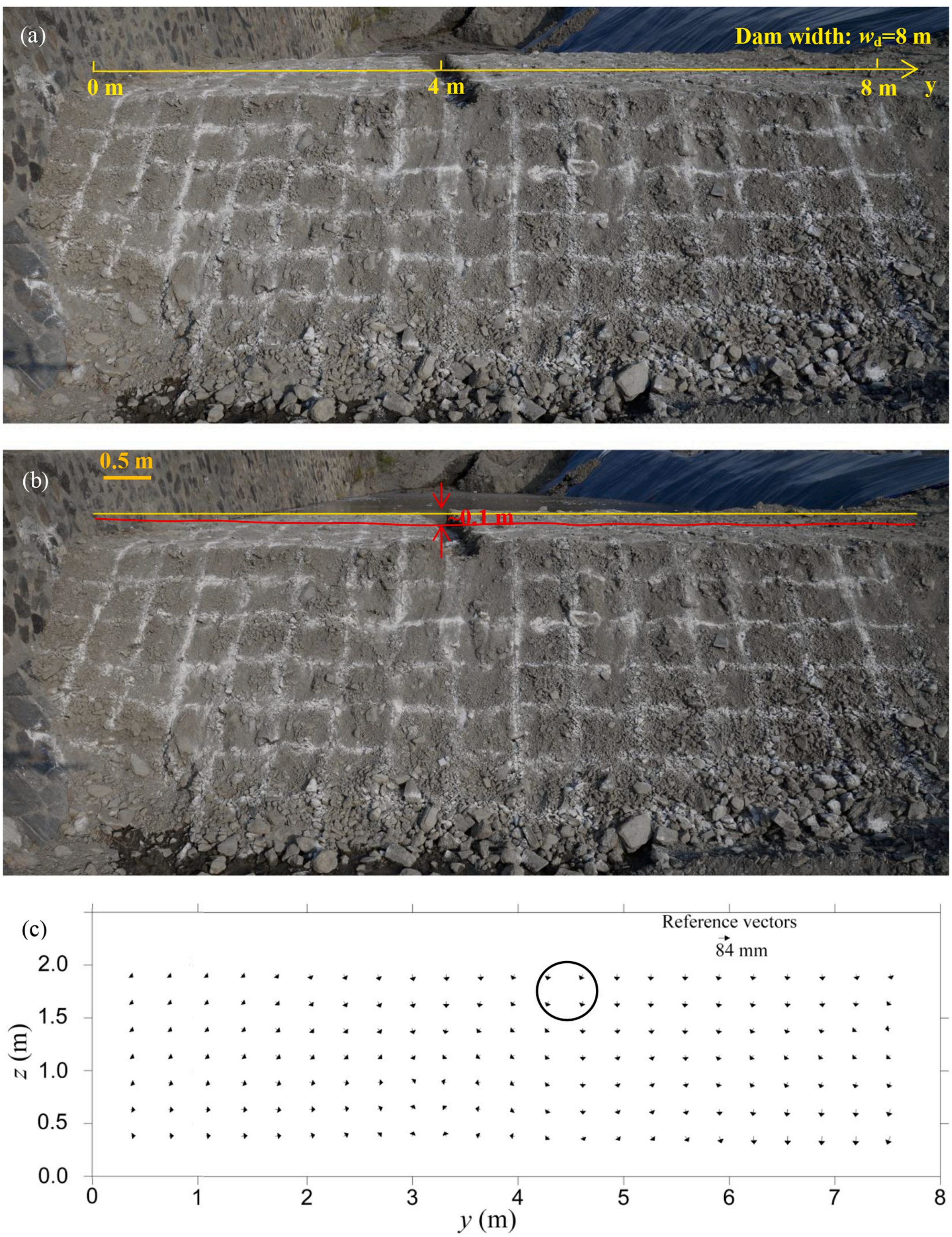

Fig. 7. The maximum deformation of dam No.1. (a) Original dam ($t = -5400$ s); (b) uneven settlement of the dam from the experimental results; (c) uneven settlement of dam from PIV analysis. The black circle indicates the maximum displacement.

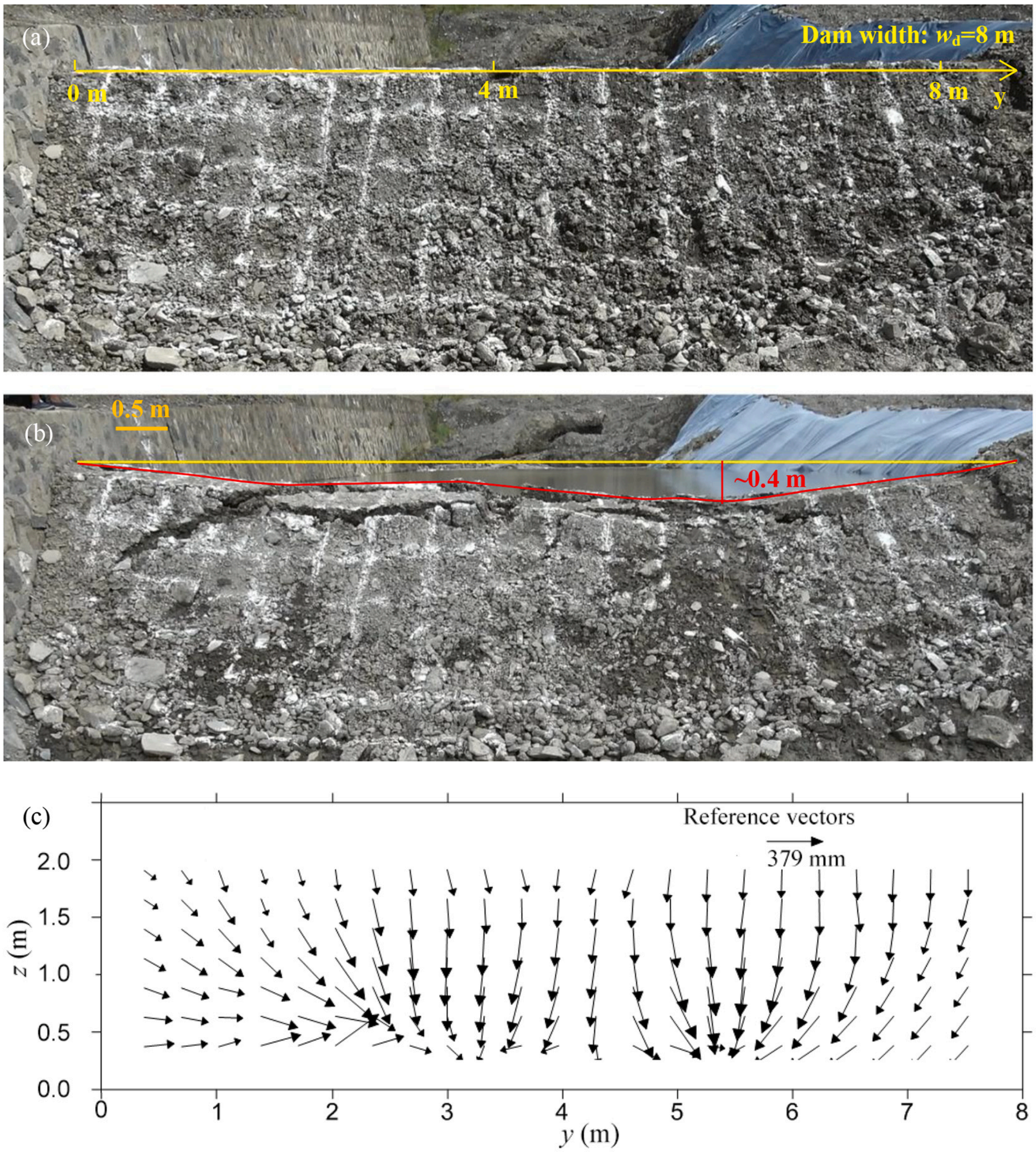

Fig. 8. The maximum deformation of dam No. 2. (a) Original dam (t = −5400 s); (b) uneven settlement of the dam from the experimental results; (c) uneven settlement of the dam from PIV analysis.

Different from Dam No. 1, wherein the maximum settlement point is located close to the notch (Fig. 7b), the observed position of maximum settlement in Dam No. 2 is situated ~2 m away from the notch (Fig. 8b), specifically at y = 6 m near the left bank, which is attributed to significant heterogeneous settlement. The time series of the complex deformation process of Dam No. 2 is shown in Fig. 9. We observed a seepage spill point emerge downstream of the dam toe (Fig. 9b, t = −5270 s) after about 130 s. At t = −2178 s, a visible uneven settlement of the dam and a seepage flow runoff on the downstream channel bed occurs (Fig. 9c). A crack gap emerges at the right shoulder of the dam because of significant seepage flow (Fig. 9d, t = −1870 s). As seepage flow and soil erosion progress, more cracks develop inside the dam body, promoting more seepage. Abundant water is observed in the middle of the downstream dam surface and at the dam toe (Fig. 9e, t = −58 s). After less than a minute, the initial erosion Point A appears at the downstream dam crest, coinciding with the location where the maximum vertical settlement is observed. Breach failure is observed a few seconds later (Fig. 9f, t = 0 s).

3.2. Processes of the dam breach

3.2.1. Morphological evolution of the breach channel

The rapid changes in the hydrodynamic conditions make the dam breaching process very complex. In Dam No. 1, seepage flow was absent on the downstream slope surface before the breach occurredher (Fig. 10a). Here, the initial time of dam breaching t = 0 s is when the water reaches the downstream dam shoulder Point A (Fig. 10a). Subsequently, the landslide dam undergoes progressive head-cut erosion and overtopping failure. The soil in the notch is gradually washed away by water, causing the erosion point to move to Point B (Fig. 10b, t = 24 s). A shallow rectangular incision along the downstream slope surface is observed, which is consistent with the SMPDBK mode proposed by Wetmore and Fread (1981), and the NWS Breach mode proposed by Fread (1988) and Macchione (2008). The eroded sediments stop at the toe of the dam and develop into a deposit fan. The increased overtopping flow depth and enhanced hydrodynamic energy move the erosion point upstream to Point C (Fig. 10c, t = 27 s). The soils on both sides of the breach become increasingly unstable and collapse at small scales

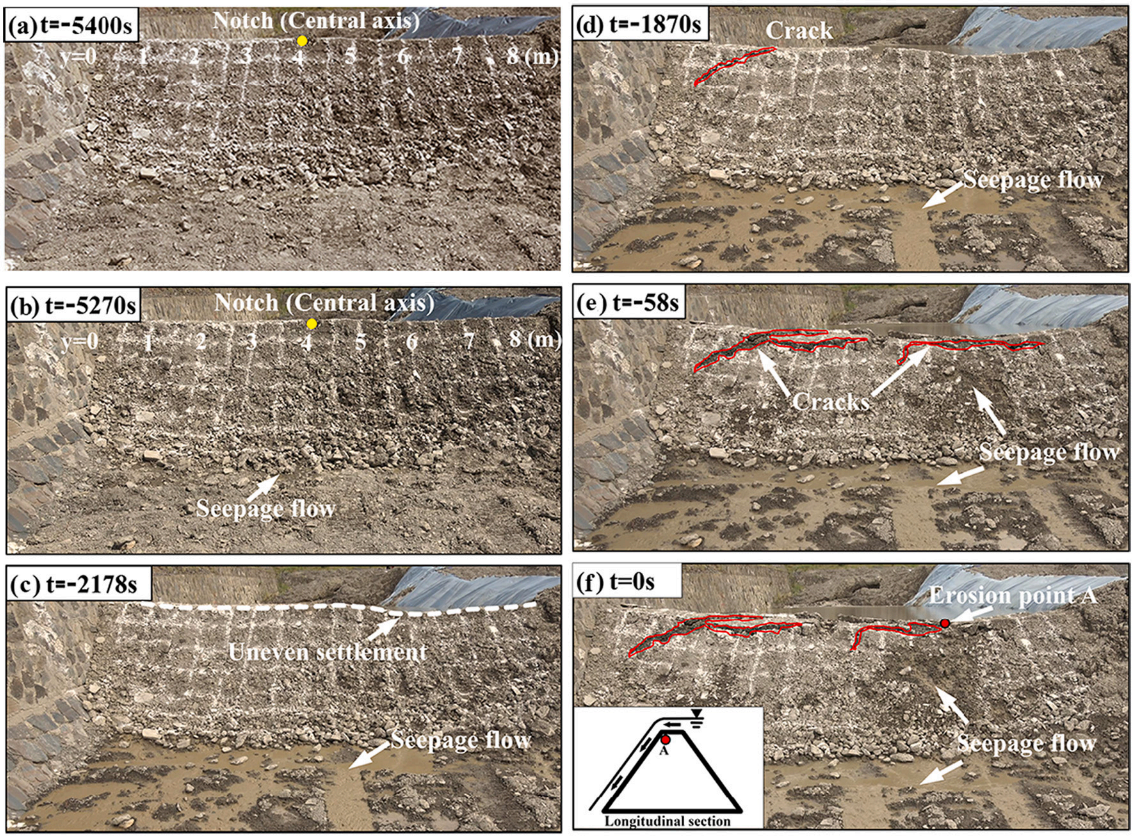

Fig. 9. Deformation process of dam No. 2 prior to dam breaching.

changing the rectangular cutting pattern to a sawtooth pattern. In addition, the collapsed soils mix with the water to form debris flows. The velocity and discharge of debris flows are relatively small, unable to move the soils at large distances. This results in the deposition of particles at the dam toe, which effectively enlarges the deposit fan (Fig. 10d). The erosion point continues to move along the dam crest towards point D (Fig. 10d, $t = 183$ s) due to the continued increase of the outburst flow. The breach area is greatly enlarged due to the large-scale collapses on both sides of the breach. Although parts of the collapsed soils are still deposited at the dam toe, they are rapidly scoured by the outburst of floods. With the increase of the breach area, the hydrodynamic energy is enhanced, driving the erosion point further upstream towards the dam shoulder Point E (Fig. 10e, $t = 452$ s). Meanwhile, the deposit fan gradually shrinks and is eventually washed away by the flow. The breach develops across the whole dam body forming a bell-shaped geometry. The outburst flooding rapidly grows and reaches its peak flow in a short time. The flow velocity is sufficiently high to erode the soils on both sides of the breach. The upstream and downstream breach widths and areas simultaneously increase and reach peak values (see Fig. 10f, $t = 710$ s. S_u, S_d denote the upstream and downstream cross-section area, respectively). The outburst discharge then gradually decreases due to the declining upstream water level. The breach width and area cease to grow, and a stable dam shape is achieved (Fig. 10g, $t = 760$ s). Finally, the hydrodynamic energy is weakened and insufficient to scour the breach's slope further, resulting in a trapezoidal profile with a side slope angle of $\beta = 54^\circ$ (Fig. 10h, $t = 1500$ s).

For Dam No. 2, seepage flows emerge before breaching at the downstream dam toe (Fig. 11a, $t = 0$ s). At the beginning of the breach, the surface soils downstream are gradually scoured by the flow having low hydrodynamic energy. Like to Dam No. 1, soils mix with the water flow to generate debris flows, which eventually deposit at the dam toe forming a debris fan (Fig. 11b, $t = 34$ s). The process of deposit fan formation lasts for about 4–5 min for Dam No. 1 but is less than 30 s for Dam No. 2. Soils on both sides slide along the exposed breach surface, resulting in a narrow rectangular channel (Fig. 11c, $t = 44$ s). Meanwhile, the erosion point migrates quickly from point B to point C along the downstream slope, and the outburst flood rapidly washes away the debris fan. The increased strength of the outburst discharge drives the erosion point down towards the dam toe (Point D) at $t = 60$ s (Fig. 11d) and is followed by a rapid increase in the outburst discharge. With time, the erosion point moves to Point E (Fig. 11e, $t = 97$ s), accompanied by the continued decrease of the reservoir water level. Subsequently, the rapidly growing flooding discharge reaches the maximum value in a very short period. The strong flow washes away the dam sediments, resulting in a sharp increase in the breach width and area. Large-scale sliding occurs on both sides of the channel and causes rapid lateral widening, corresponding to a rapid rise in the breach area (Fig. 11f, $t = 180$ s and Fig. 11g, $t = 240$ s). Eventually, a wide breach forms and the upstream water level gradually decreases due to weak hydrodynamic conditions and attenuated soil erosion. Dam failure ends when the resistive force of soils balances the erosive force of the outburst flood, leaving a trapezoidal breach cross-section with a side slope angle $\beta = 45^\circ$ (Fig. 11h, $t = 540$ s). This is notably smaller than the side slope angle in Dam No. 1 (Fig. 10h).

In addition, we observe that the side slope evolution processes during breaching are different for the two dams. Fig. 12 illustrates the modes of collapse at the side slope for both model dams. For Dam No. 1, masses or chunks of soil material remain suspended on the slope surface (Fig. 12a) until its self-weight overcomes the matric suction that keeps it in place, causing it to fall into the water (Fig. 12b). In Dam No. 1, the soil clusters easily slide along the slope and into the flowing water (Fig. 12c and d). The lateral erosion of Dam No. 1 is a combination of continuous erosion and episodes of sudden collapses. In contrast, the lateral erosion of Dam No. 2 is a combination of constant erosion and episodic sliding.

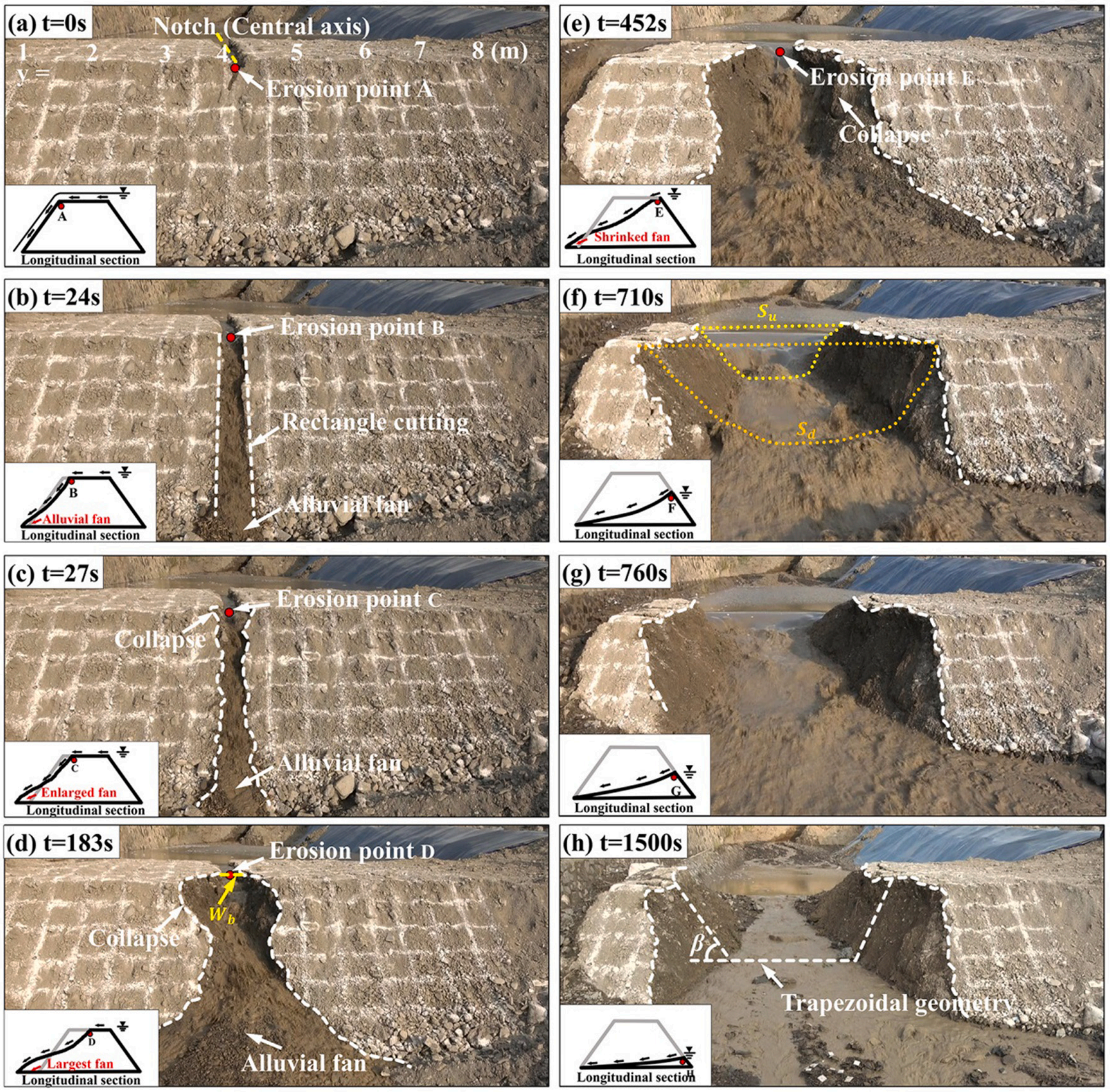

Fig. 10. The breaching process for dam No. 1. Erosion point indicates the initiation of headcut.

3.2.2. *Hydrological process of outburst flooding*

For landslide dam failure, the water volume balance equation can be approximated as:

$$\frac{dV_L}{dt} = Q_{in} - Q \tag{3}$$

where Q is the breach outflow discharge, V_L is the volume that is a function of upstream headwater level, t is time, and Q_{in} is the inflow discharge. The upstream inflow is considered to be a steady-state flow with a constant discharge of about 0.1 m^3/s in this study. The estimated hydrograph of the outburst flood is shown in Fig. 13a. The duration of the failure time for Dam No. 1 (1500 s) is about three times longer than that of Dam No. 2 (540 s), but the peak discharge of Dam No. 2 (3.38 m^3/s) is about twice larger than that of Dam No. 1 (1.77 m^3/s). The results suggest that the breach process of Dam No. 2 is more rapid than in Dam No. 1. The breach parameters such as the cross-sectional area S_b, breach width w_b, and side slope angle β are illustrated in Fig. 13b, c, and d, respectively. According to the hydrograph profiles, the landslide dam failure can be divided into three stages:

Stage 1: Initiation of the dam breach. A stream of water escapes from the reservoir and slowly initiates the overtopping flows across the dam crest. Due to the relatively small flow velocity, discharge, and weak erosive force from the outburst flood, the changes of the breach area S_b and breach width w_b are both relatively small (Fig. 13b and c). Meanwhile, the flood gradually incises the downstream dam surface, leading to a narrow channel with almost vertical banks (i.e., the side slope of the breach is nearly 90°). This process lasts for 500 s for Dam No. 1 but lasts no more than 90 s for Dam No. 2 (Fig. 13d).

Stage 2: Rapid increase of outburst floods. Outburst floods flow over the dam crest, and the head-cut continues along the entire width. The undercut breach progressively lengthens and widens (Fig. 13c), accompanied by a rapid increase in discharge (Fig. 13a). At this stage, the failure is mainly caused by soil collapses or sliding due to lateral incisions from the flow. The variation of the side slope fluctuates due to the random slumping of soil blocks from the dam. The side slope β varies between the ranges of 50° - 60° and 43° - 54° for dams No.1 and No. 2, respectively (Fig. 13d). In addition, the breach area S_d at the downstream shoulder develops earlier and faster than the upstream shoulder S_u for Dam No. 1 (Fig. 13b). This further proves that the breach develops gradually from the downstream shoulder towards the upstream.

Stage 3: Attenuation of outburst floods. As the upstream water level decreases and the breach further enlarges, the outburst discharge gradually decreases (Fig. 13a). The kinetic energy of the flood is now too small to overcome the resistance of soils and could not further trigger slope failures. Variation in the breach area S_b (Fig. 13b) and the side

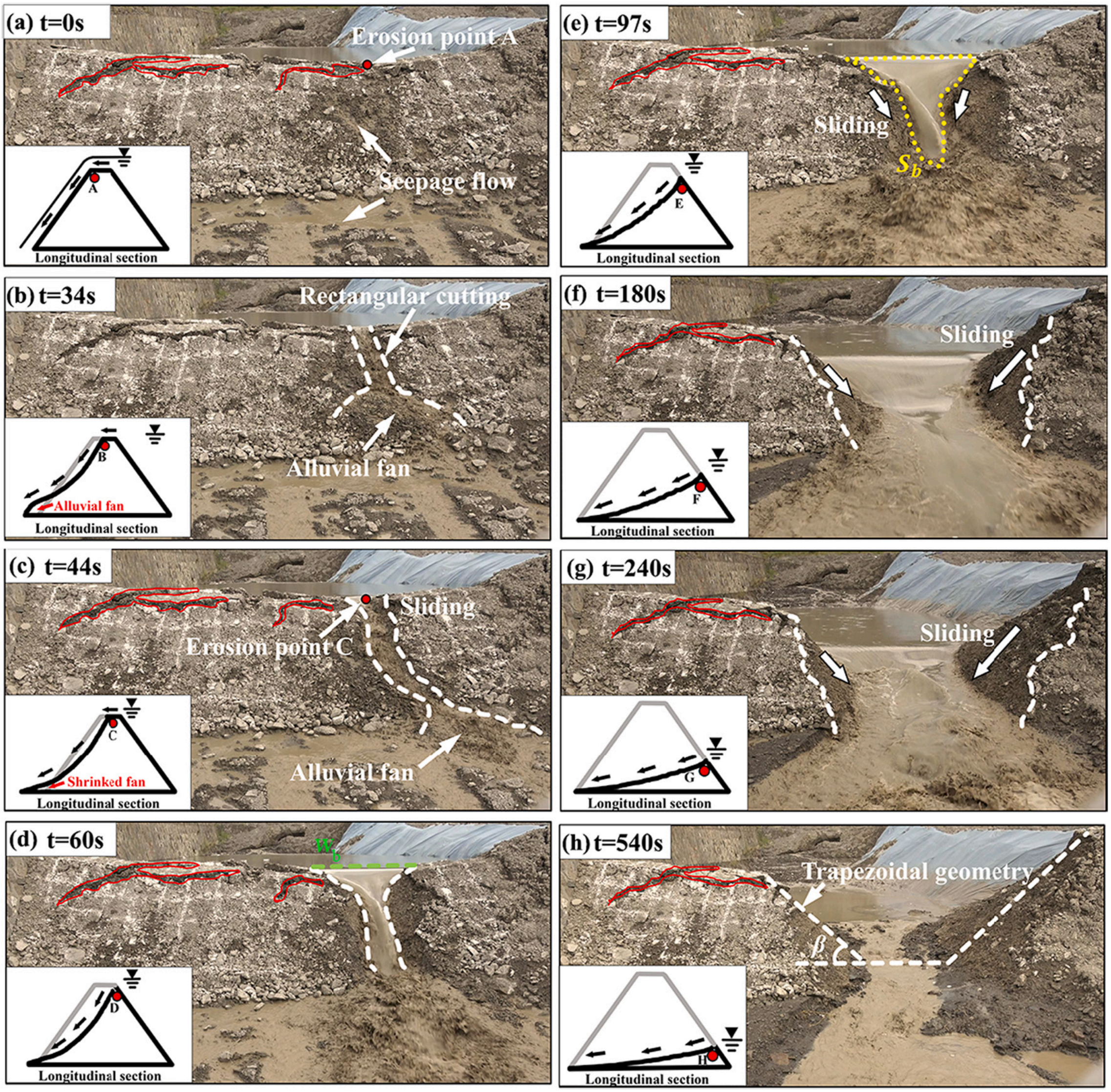

Fig. 11. The breaching process for dam No. 2.

slope angle β (Fig. 13d) are now minimal. The residual side slope angle β for Dam No. 1 is larger than Dam No. 2 (Fig. 13d). These three stages of landslide dam failure are consistent with the variations of breach area, breach width, side slope angle, and outburst discharge.

3.2.3. *Hydraulic Characteristics of the Breach Crest*

The dam breach process is a complex spatial-temporal phenomenon, making it challenging to model physically. The time-dependent hydrograph of outburst flow for dam breach (e.g., Eq. (3)) is one method used to calculate the outflow discharge. On the other hand, because the water flow over the landslide dam crest is similar to the flow over a broad-crest weir, the broad crested weir equation is adopted to estimate the outflow discharge and can be written as (Chanson, 2004):

$$Q = C_D\sqrt{g}\left(\tfrac{2}{3}H\right)^{3/2} \tag{4}$$

where C_D is the discharge coefficient, g is the acceleration due to gravity, and H is the total headwater. The coefficient $(2/3)^{3/2}$ is derived from the analysis of the ideal broad-crested weir (Chanson, 2004, pp. 395–397).

Moreover, based on the investigation of numerous dam failures, some researchers (e.g., Johnson and Illes, 1976; Singh and Snorrason, 1984; FERC, 1987; Trieste, 1988) found that the width of the breach crest w_b is normally 0.5 to 5.0 times greater the breach depth H_d. Generally, H_d can be approximated as the headwater H for landslide dams when overtopping failure occurs. The correlation between w_b and H_d allows for the direct estimation of the outflow discharge Q through w_b. The photogrammetry and pebble-motion analyses similar to those in Walder et al. (2015) are applied to describe the breach shape and evolution over time quantitatively (see Fig. 14). Here, the straight-line distance between the ends of the breach crest is w_b (see Fig. 13c and d). Red arrows point to the direction of the transition of the discharge behavior between Stages 2 and 3. It can be observed that w_b is positively correlated to Q in Stages 1 and 2, where the discharge is still increasing towards a maximum value. From this trend, the relationship between Q, and w_b can be defined as:

$$w_b = 3.03\left(Q^2/g\right)^{1/5} \tag{5}$$

This sharp increase of w_b with increasing Q agrees well with Walder et al. (2015). The close agreement is interesting since results from Walder et al. (2015) involve sediments with $d_{50} = 0.21$ mm, which is considerably finer than the experiments of this study.

From Figs. 13c and 14, it is also noted that w_b slowly and slightly decreases with decreasing Q at Stage 3. This is because the breach crest is not a feature of equilibrium morphology. Since w_b primarily reflects

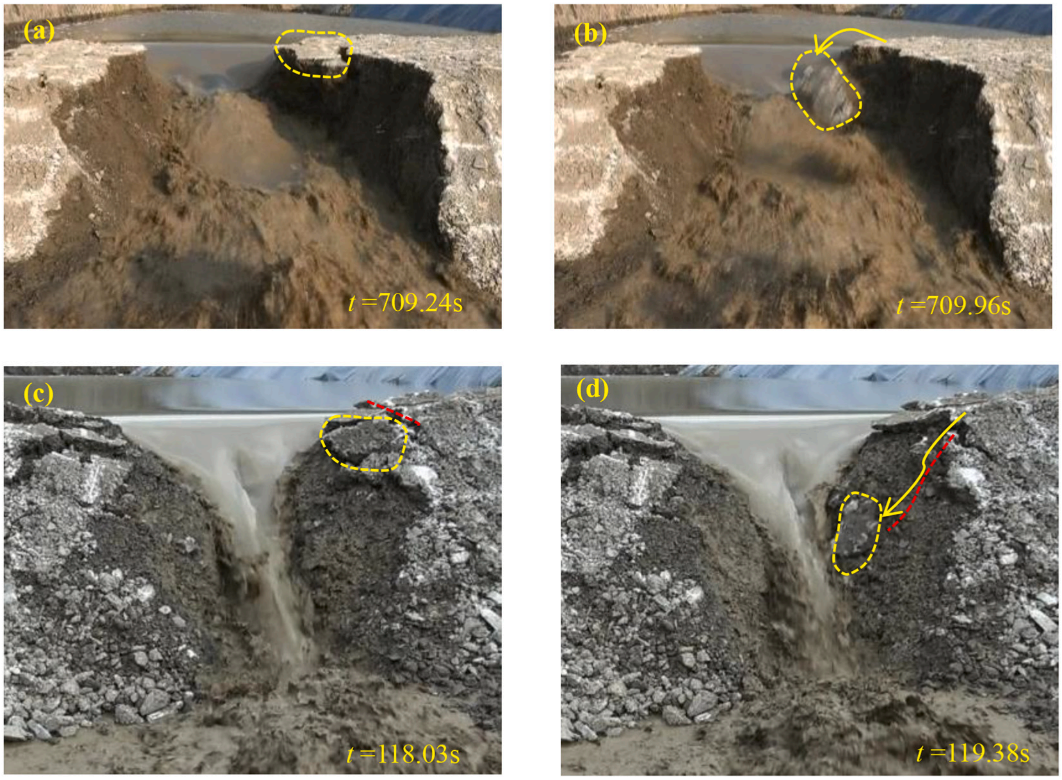

Fig. 12. Snapshots of the typical lateral breach process for dams (a-b) No.1 and (c-d) No. 2.

traction erosion and disturbance caused by slope failure, it may decrease with the hydrodynamic energy because of the decreasing outflow discharge. Furthermore, the breach width w (as a proxy for w_b) measured at the top of the breach crest can also be considered a measure of the breach-channel width shaped primarily by the slope failures. It is relatively easy to determine w from the photographs obtained from cameras. Unlike the variation of w_b with Q at Stage 3, w continues to grow due to the episodic slope failures even after the outflow discharge decreases at Stage 3.

The grain size distributions of dam soil are another potential factor influencing the outburst flood. For example, Pickert et al. (2011) conducted experiments and concluded that coarser materials could result in a faster breaching process. However, Schmocker and Hager (2012) pointed out that the erosion process slowed down with the increased sediment size after the initial overtopping phase. Hakimzadeh et al. (2014) also showed that as d_{50} increased from 0.25 to 2 mm, the peak flow decreased slightly. We analyze the dependence of the breaching process on the grain size using data obtained from this study ($d_{50} = 12.4$ mm) as well as from the data of Coleman et al. (2002) (d_{50} = 0.5–2.4 mm) and Walder et al. (2015) ($d_{50} = 0.21$ mm). As illustrated in Fig. 15, good agreement is observed between the measurements obtained from Dam No. 2 and the data of Coleman et al. (2002) and Walder et al. (2015). The data fall within the 90% confidence interval (see the light grey band in Fig. 15) of the best-fit equation:

$$log\left(\frac{Q}{g^{1/2}{d_{50}}^{5/2}}\right) = 2.5log\left(\frac{w_b}{d_{50}}\right) - 1.78 \tag{6}$$

which is equivalent to

$$Q = 0.016g^{1/2}{w_b}^{5/2} \tag{7}$$

Eq. (7) indicates that d_{50} has less influence on the outflow discharge Q for Dam No. 2 than for Dam No. 1. A different best-fit equation for Dam No. 1 is obtained and is formally written as:

$$log\left(\frac{Q}{g^{1/2}{d_{50}}^{5/2}}\right) = 1.36log\left(\frac{w_b}{d_{50}}\right) + 1.23 \tag{8}$$

which can be re-arranged to yield:

$$Q = 16.982g^{1/2}{w_b}^{5/2}\left(\frac{d_{50}}{w_b}\right)^{1.14} \tag{9}$$

Eq. (9) implies that the outflow discharge for Dam No. 1 has a positive relationship with the mean particle diameter (d_{50}).

3.3. *Influence of outburst flood on channel morphology*

The channel topographies downstream before and after the dam failure are obtained by a 3D scanner. The topography differences are estimated and are projected as contour maps in Fig. 16. The positive values represent deposition, while the negative values represent erosion. A clear difference is observed between the deposits of these two dams. For Dam No. 1, deposition dominates at the dam toe, which is evident until $x = 15$ m. Farther away from the dam, obvious signs of erosion can be observed with limited local accumulation. For Dam No. 2, the downstream channel is mainly scoured for the first 15 m, after which deposition gradually develops along the flow direction.

Fig. 17a and b compare the initial and final topographies of the longitudinal profiles of dams No. 1 and 2 as well as their difference along the center of the breach. Generally, linear bed profiles are observed before and after the failure of both dams. Although the inflow rate, upstream water level, storage capacity, and granular materials of the two dams are the same, the ranges of deposition (above the dashed line) and erosion (below the dashed line) occur at different positions. This may be attributed to the difference in the hydrographs of the dams. For Dam No. 1, a relatively low outburst flow rate and a long breach time limit the ability of the breach floods to scour the downstream channel, especially at Stage 3, resulting in the dominance of deposition behind the dam. However, the failure of Dam No. 2 is rapid, which effectively

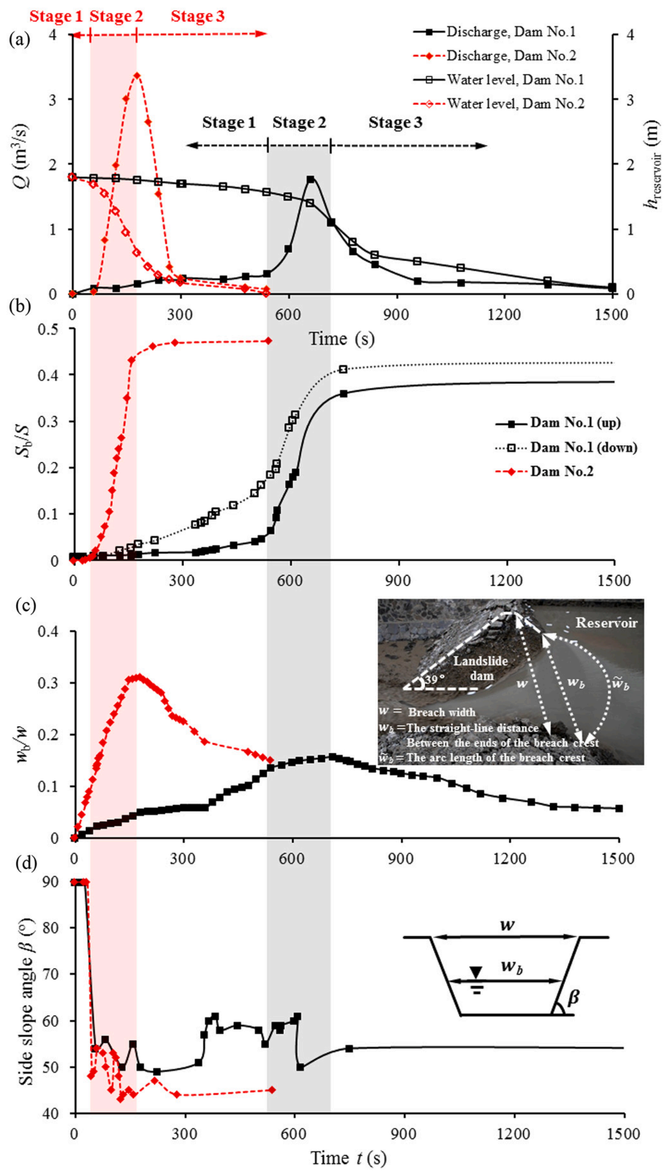

Fig. 13. Hydrological evolution of landslide dam breaching defined through the (a) outburst discharge and the reservoir water level, (b) breach area, (c) straight-line distance of breach, and (d) side slope of the breach.

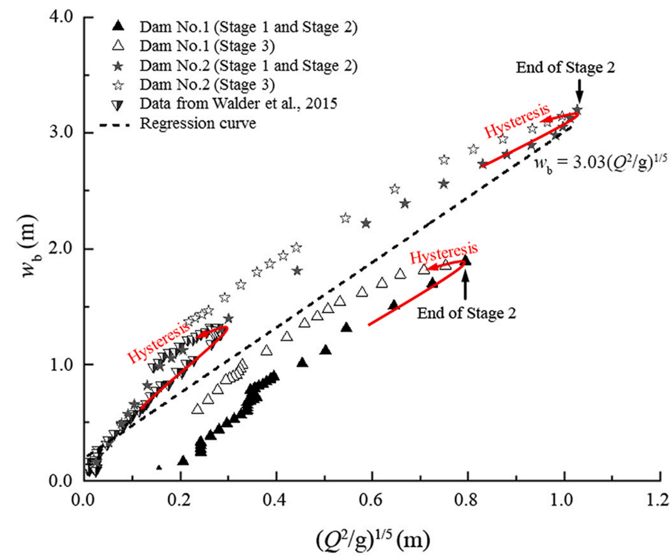

Fig. 14. Relationship between breach width$w_b$and outflow discharge. Arrows indicate the direction of the change in discharge with time.

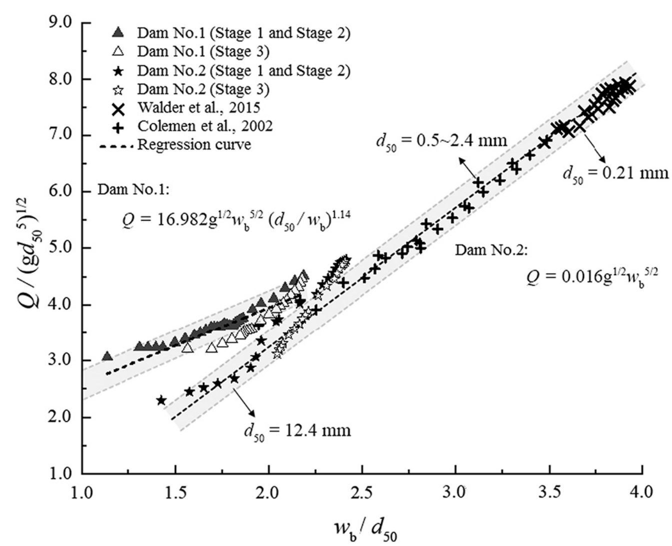

Fig. 15. Dimensionless outflow discharge ($Q/\sqrt{gd_{50}^5}$) as a function of the dimensionless breach crest width (w_b/d_{50}) in log-scale.

results in a peak discharge that is larger than that of Dam No. 1. The outburst flow scours the downstream channel, especially at the dam toe. This is followed by the gradual reduction of the flow velocity and deposition of soil material along the channel. The results indicate that the magnitude of the outburst of floods from the landslide dam failure significantly influences the downstream channel topography.

We also analyze the variation of the particle composition at the downstream channel bed from $x = 0$ m to $x = 35$ m before and after dam failure. Fig. 17c and d show the characteristics of the grain size distributions (d_5, d_{16}, d_{50}, d_{84}, and d_{95}) and sorting indices. Particle sizes (both fine and coarse) are found to vary periodically along the channel bed. Although most grain sizes along the flow direction at the post-failure channel bed, are smaller than the original materials at the channel bed, they do not follow an exponential (or linear) decline. In other words, grain sizes do not significantly decrease along flow direction (i.e., lack of downstream fining). The change of grain sizes along the longitudinal direction can be described as a sinusoidal function of the form:

$$\frac{d_i}{d_o} = A\sin\left(\frac{2\pi}{T}\boldsymbol{x} + \boldsymbol{\beta}\right) + \boldsymbol{\alpha} \tag{10}$$

where x denotes the downstream distance from the dam, A is the amplitude of the variation, $2\pi/T$ is the frequency, T is the period of the variation, β is the phase angle, and α represents the average value around which the data varies. The sum of the squared error (SSE $= \sum_{i=1}^{n} w_i (d_i/d_o - \overline{d_i/d_o})^2$) is used to quantify the fitness of the curves for each mean grain size. The possible range of SSE is $[0, +\infty]$, where an SSE of zero indicates a highly optimized fitting. All parameter values are shown in Fig. 17c.

Results show that the period of variation for each particle size is similar (~6.0 m) for both dams, although the T value of Dam No.1 is slightly lower (~11%) than that of Dam No.2. The value of β is different for the two dams, indicating that the shifted positions of the curves relative to the origin are dissimilar. The curves for Dam No.1 have larger values of A and α relative to Dam No.2, which suggests that bed particles

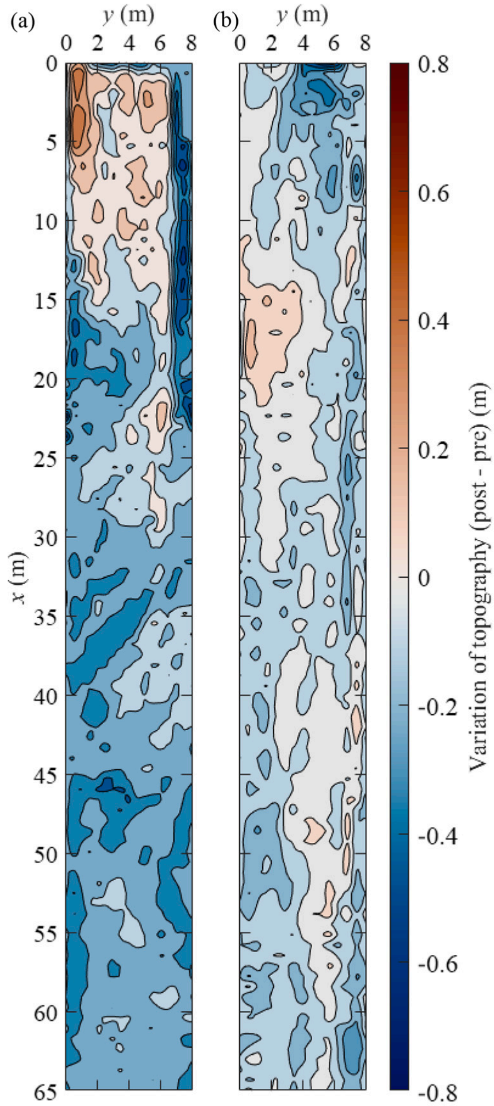

Fig. 16. Variation of the bed topography at the downstream channel of (a) dam No. 1 and (b) dam No. 2.

downstream Dam No.2 are better sorted than Dam No.1. Thus, to a certain extent, the difference in the hydrological processes of the two collapsed dams is reflected in their respective modes of grain size variation. The fluctuation of particle size along the channel bed can be attributed to the oscillatory motion of the outburst flood and is an externalization of the fluid inertia. Unsteady and non-uniform outburst floods continue to erode the dam and entrain particles of different sizes onto the river bed, resulting in a poor sorting phenomenon. The value of the invariable sorting index (~1.7) also verifies the limited degree of fining (Fig. 17d).

4. Discussion

4.1. Two different failure mechanisms

From the experimental results presented in the preceding chapters, significant differences are observed between the deformation, the outburst flooding, and the downstream channel morphology of the two landslide dams. Here, we try to explore the differences in their settlement deformation. The two dams have the same height and material composition, experience the same inflow discharge, and are distinct only in their length L_b. This difference can influence the seepage flow, in other words, the path the water takes while inside the dam body.

Based on Darcy's law, which defines the relationship between the hydraulic conductivity and the hydraulic permeability (Yolcubal et al., 2004), and the Hazen approximation (Hazen, 1911; Krumbein, 1934; Alyamani and Sen, 1993), the flow discharge through a porous medium of soils can be expressed as:

$$q = C{d_{10}}^2\frac{\rho g}{\mu}\frac{\Delta h}{\Delta L} \tag{11}$$

where, C is a coefficient that reflects the soil characteristics, such as packing geometry, grain morphology, pore size, and grain-size distribution. d_{10} is the diameter of the tenth percentile (by weight) grain size of the soil, ρ is the fluid density, g is the gravitational acceleration, μ is the dynamic viscosity, Δh is the total water head difference along with the seepage distance (ΔL). The ratio of water head difference and its horizontal exfiltration length is the hydraulic gradient ($j = \Delta h/\Delta L$). For the two dams constructed in this study, the parameters in Eq. (11) that affect seepage flow discharge are almost identical except for the seepage path length (ΔL). The seepage path length (ΔL) in Dam No. 1 is nearly 1.8 times longer than in Dam No. 2, resulting in greater seepage discharge for Dam No. 2.

We used a commercially available finite-element hydrology program SEEP/W, which is a part of the Geo-Studio software (Geo-Slope International Ltd., https://www.geoslope.com/products/geostudio), to conduct transient seepage analysis. The transient seepage calculation for 2D unsaturated soils is based on Richards' equation (Richards, 1931),

$$\frac{\partial}{\partial x}\left(k_x\frac{\partial H}{\partial x}\right) + \frac{\partial}{\partial z}\left(k_z\frac{\partial H}{\partial z}\right) + Q_s = m_{\mathrm{w}}\gamma_{\mathrm{w}}\frac{\partial H}{\partial t} \tag{12}$$

where k_x and k_z are the permeability coefficients parallel (x) and perpendicular (z) to the flow direction, respectively. H is the total water head, which is the sum of the elevation head, pressure head, and velocity head. Q_s is the applied boundary flux, m_{w} is the slope of the volumetric water retention curve (SWCC), γ_{w} is the unit weight of water, and t is the time.

The geometry of the simulated dams is identical to those adopted in the experiments. Recall that in the experiments, the water level reaches the notch ($H = 1.8$ m), following a constant inflow discharge of $\approx 0.1\mathrm{m}^3/\mathrm{s}$, in $t = 5400$ s. The same inflow conditions are adopted in the simulations to maintain consistency. The unsaturated soil properties defined through experiments (SWCC curve of bulk density of 1570 kg/m^3 in Fig. 6) are also used as inputs for the simulation. As direct measurement of the permeability of unsaturated soils is time-consuming and costly when conducted in the field, we only tested the saturated permeability of the soil (2.89 e-05 m/s). The method proposed by Fredlund et al. (1994) is then used to estimate the hydraulic permeability function based on the SWCC. The SWCC and hydraulic permeability functions used in the numerical simulation are summarized in Table 2. In addition, the potential seepage face is on the downstream dam surface. Downstream of the dam toe, a zero pressure head boundary condition is assigned to the ground surface. The bottom of the modeled dam is also assumed to be impermeable.

The distribution of the seepage flow rate and pore water pressure inside the dam body ($t = 5400$ s) are shown in Fig. 18. The maximum seepage flow rate for the two dams is similar, and both occur at the upstream crest. The seepage flow rates decrease along the x-direction, consistent with the energy conservation. However, we observed some differences between the two dams. Firstly, the phreatic water surface inside Dam No. 1 only reached the downstream dam toe (Fig. 18a1), whereas the flow permeated throughout the dam body and reached the middle of the downstream dam face in Dam No. 2 (Fig. 18b1). Secondly, the seepage flow rates at the downstream toe of Dam No. 1 are close to zero, whereas they are approximately half of the maximum seepage flow rate at the downstream toe of Dam No. 2. These results agree with the seepage exposed position observed in the experimental tests (Figs. 10a

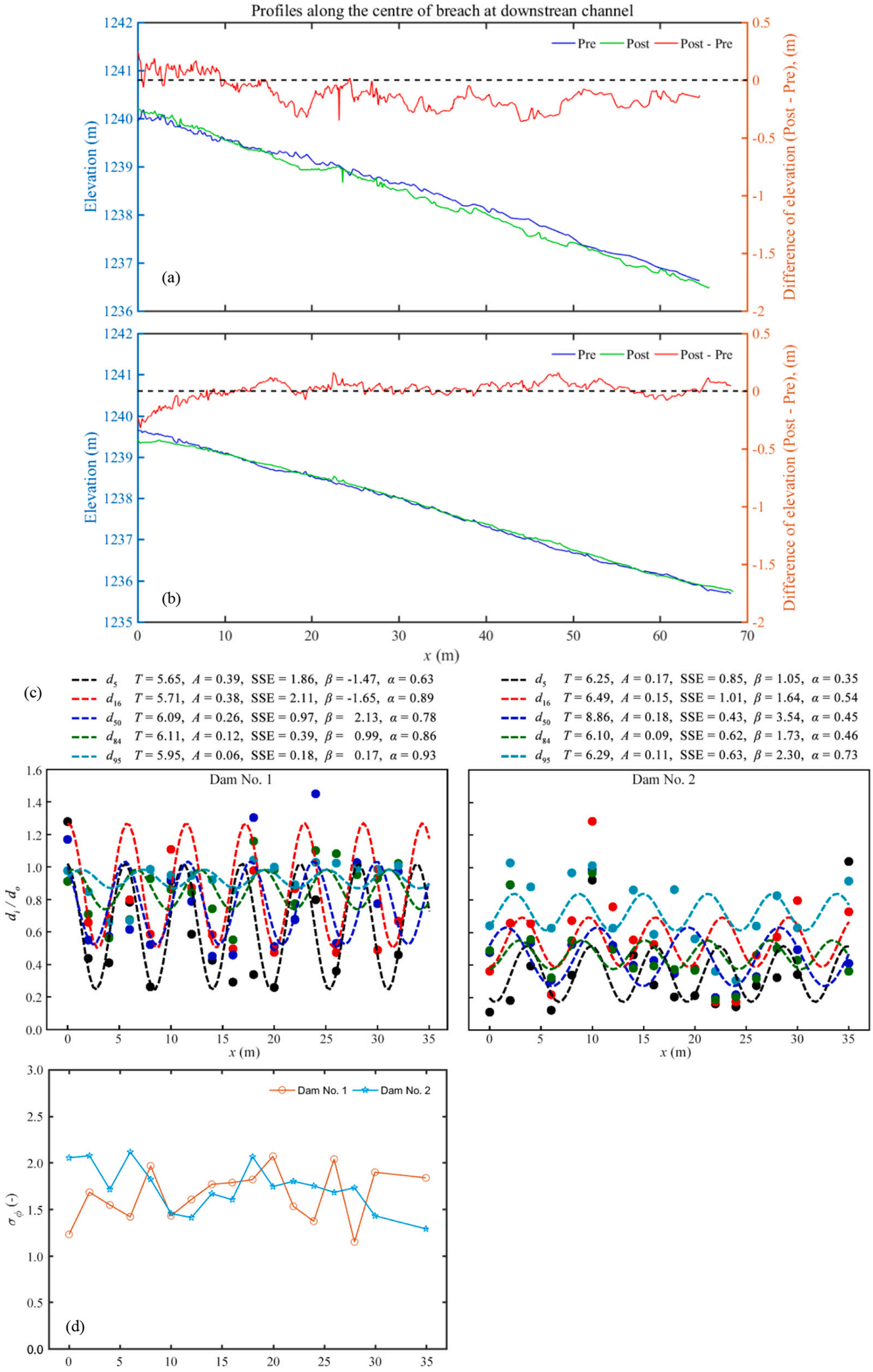

Fig. 17. Downstream variations in elevation for dams (a) No.1 (y = 4.0 m) and (b) No. 2 (y = 6.0 m). (c) Periodic variation in the typical particle sizes and (d) the distribution of sorting index along the center of the breach from 0 to 35 m.

Table 2
Soil parameters used in the seepage numerical model.

Soil-water characteristic curve (SWCC)		Hydraulic permeability functions[a]	
Volumetric water content	Matrix suction (kPa)	Hydraulic conductivity in x- and z- direction, $K_x = K_z$ (m/s)	Matrix suction (kPa)
0.39892	0.10	2.89e-05	0.00
0.38047	4.00	2.10e-05	0.10
0.36607	6.00	1.70e-05	0.34
0.34353	12.00	1.15e-05	1.11
0.30836	25.00	5.37e-06	3.60
0.24056	50.00	1.14e-06	11.70
0.18643	100.00	8.44e-08	37.96
0.15558	200.00	3.24e-09	123.23
0.14894	400.00	1.02e-10	400.00

[a] Note: the hydraulic permeability function was obtained using the method of Fredlund et al. (1994).

and 11a). Thirdly, most parts of Dam No. 1 endure negative pore pressures (Fig. 18a2, unsaturated state), whereas pore pressure is mostly positive within the body of Dam No. 2 (Fig. 18b2, saturated state). This is consistent with previous research wherein seepage flow is found to increase positive pore pressures in saturated soils (Fredlund, 2006). The results indicate that there is minimal seepage flows in Dam No. 1, whereas seepage flows are intense in Dam No. 2.

The mass fraction of fines content (<0.063 mm) is 3.89%, less than 5%; and the ratio of $(C_H/C_F)_{\min} = 0.63 < 1.0$ (C_F = mass fraction of particles finer than grain size d, C_H = mass fraction of particles ranging from d to $4d$). According to the geometric criteria proposed by Chang and Zhang (2013b), Well-graded materials are internally unstable. For internally unstable materials, once the fine particles are washed away, the permeability of the material increases, which may induce the reduction of the shear strength, resulting in the dam's failure.

During steady-state seepage, the change from being unsaturated to a saturated state induces high hydraulic gradients, reducing soil cohesion. This increases the force that accelerates soil movement, exfiltration, and entrainment. Such force can be described by the expression previously developed by Cheng and Chiew (1999):

$$F_{SS} = \frac{j\rho g\pi d^3}{6(1-\varepsilon)} \tag{13}$$

where F_{ss} is seepage force per unit volume, $\varepsilon$is the porosity, and d is the particle diameter. The seepage force is influenced by the hydraulic gradient (i.e., $j = \Delta h/\Delta L$) and the porosity. A large hydraulic gradient in Dam No. 2 may result in high seepage flow discharges and the washing away of fine particles. As the soil porosity increases, seepage forces increase accordingly. This further promotes the erosion of soil grains and therefore influences the stability of the dam.

Seepage erosion changes landslide dam failure by altering the internal stress conditions, soil deformation, and migration of fine particles (Chen et al., 2020). In Dam No.1, the relatively long seepage path and small hydraulic gradients result in weak seepage flow. The seepage forces (Eq. 13) are too small to overcome the soil stress condition, resulting in minimal migration of fine particles and negligible dam deformation (see Fig. 7). The unsaturated soil structures maintain strong force chains that resist erosion due to overtopping flow, resulting in relatively long dam breach durations and small peak discharges (see Fig. 13). For Dam No. 2, the strong seepage flows penetrate the dam body (see Fig. 18b1) and induce the incessant saturation of soils, resulting in reduced effective stress of materials. Furthermore, the high hydraulic gradients induce the detachment and transport of fine particles. As more fine particles are washed away, force chains buckle and break from the lack of structural support, causing the dam to deform (see Fig. 8) (Chen et al., 2020). In this condition ("overtopping and seepage" failure mode), the outburst flood discharge is independent of the grain size. However, Q is observed to slightly increase with d_{50} in the overtopping failure mode (Dam No. 1) (see Fig. 15). Additional investigation is needed to verify the relationship between the discharge and grain size for each of the failure modes. Generally, seepage flows play an essential role in the failure of landslide dams: high amounts of seepage flows result in a wetter dam body and larger seepage forces which decrease the stability of the dam, accelerate the breach process, and increase the magnitude of the subsequent outburst floods. Furthermore, the flood significantly erodes the downstream channel bed. The results suggest that accounting for seepage flow in the overtopping failure is important for the proper estimation of discharge and range of inundation, both of which are necessary for developing emergency preparedness measures. When a landslide dam is identified, seepage effects need to be considered for risk management and mitigation design, especially when the incoming flows are large and the longitudinal lengths of the dams are small.

4.2. Grain size downstream fining

In outburst flood channels, the grain size downstream fining is linked to sediment sorting, channel topography, and flow patterns. Size-selective sediment entrainment based on bed shear stress or discharge provides a potential explanation for the absence of sediment fining. Grains are moved when the bed shear stress exerted on the grains is greater than a critical value. Shields (1936) proposed a dimensionless parameter (τ_c*) to assess critical flow conditions for sediment entrainment. The critical shear stress (τ_c, in N/m^2) for bed particle entrainment can be written as follows:

$$\tau_c = \tau_c^*(\rho_s - \rho_w)gd_{50} \tag{14}$$

where ρ_w and ρ_s denote the density (kg/m^3) of water and sediment, respectively. g is the acceleration due to gravity. The dimensionless Shields number (τ_c*) is calculated using the expression proposed by Ferguson (2012), which suits very steep gravel-bed rivers:

$$\tau_c^* = S^{0.32}(d_{84}/d_{50})^{0.23} \tag{15}$$

where S is the dimensionless energy gradient and is commonly approximated by the channel slope.

In addition to the Shields method, two other critical shear stress formulas, proposed by Engelund (1965) and Frings (2008), are also tested in this study:

$$\tau_{c,i} = \frac{0.1(\rho_s - \rho_w)gd_i}{\left[lg\left(19\frac{d_i}{d_{50}}\right)\right]^2} \tag{16}$$

$$\tau_{c,i} = a(\rho_s - \rho_w)gd_i\left[\frac{d_i}{d_{50}}\right]^{-\mathrm{HE}} \tag{17}$$

where d_i is the grain size of fraction i, $\tau_{c,i}$ is the critical bed shear stress for fraction i. a is an empirical constant, representing the Shields dimensionless coefficient when the sediment is homogeneous, i.e., d_i / $d_{50} = 1$. HE is the hiding-exposure coefficient, derived from the Shields function, which typically assumes values within the range from 0.29 to 1, and indicates whether entrainment is selective or equal. Equal entrainment mobility prevails if HE = 1, and the more HE deviates from 1, the stronger the degree of selective entrainment will be. Andrews (1983) obtained $a = 0.0834$ and HE = 0.872 using the data from three natural gravel-sand riverbeds composed of nonuniformly sized materials, similar to what is used in this study.

As an alternative, the critical discharge has been described as an attractive method for predicting sediment transport because it is relatively easy to obtain the inputs. The critical discharge formulas proposed by Indri (1941), Meyer-Peter et al. (1934), Bathurst et al. (1987), and Schoklitsch (1962) are computed in this study:

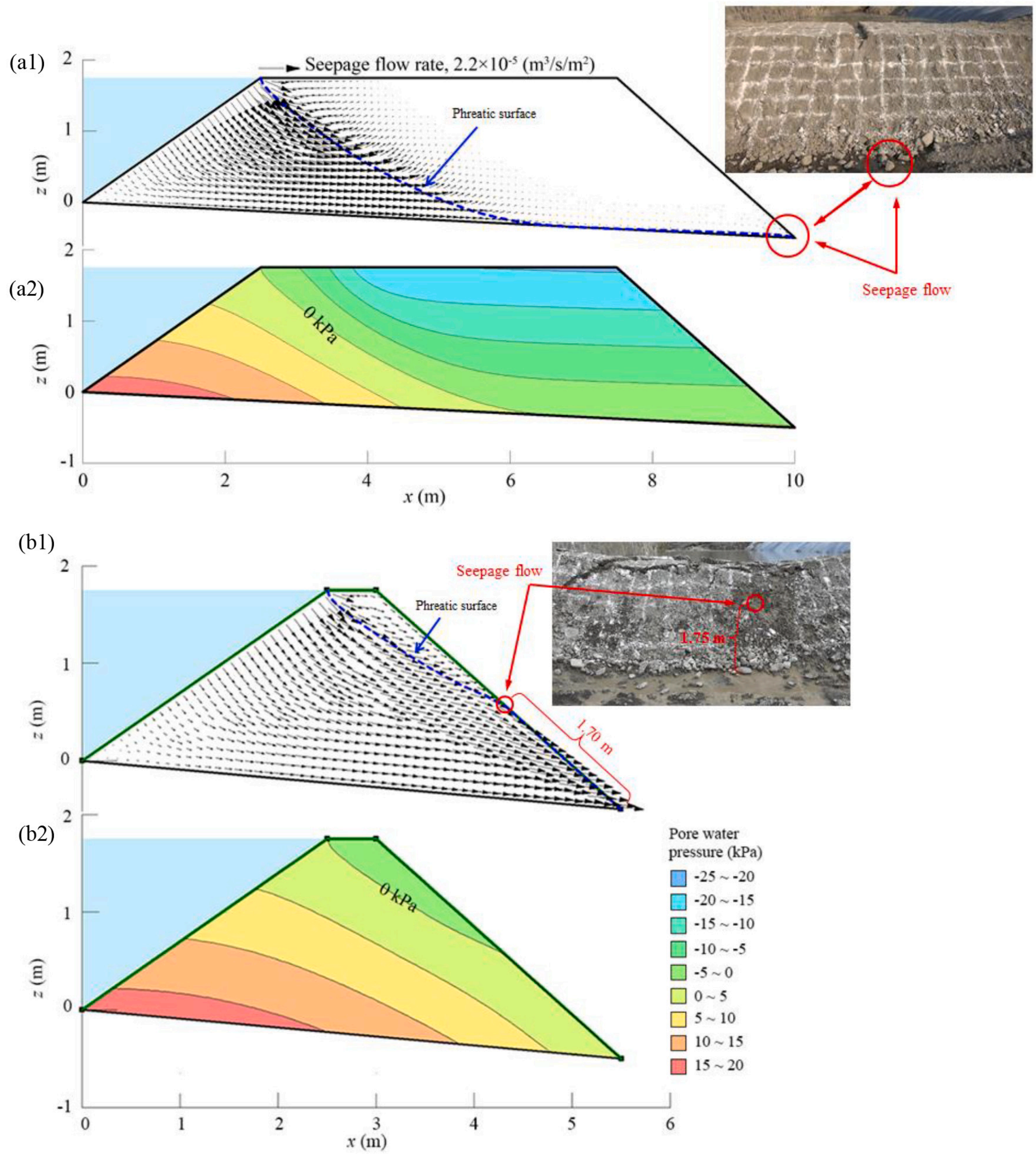

Fig. 18. The distribution of (a1 and b1) seepage rates and (a2 and b2) pore water pressures at 5400 s for dam No. 1 and dam No. 2. Field tests pictures showing the locations of seepage flow.

$$Q_c = \left[\tau_c / (\rho_w g m_1 S)\right]^{1/n_1} \tag{18}$$

$$Q_c = \left[0.07 (d_m / S)^{1.5} m_2\right]^{1/(1-n_2)} \tag{19}$$

$$Q_c = \left[0.15 g^{0.5} {d_{16}}^{1.5} S^{-1.12} m_2\right]^{1/(1-n_2)} \tag{20}$$

$$Q_c = \left\{0.26\left[(\rho_s - \rho_w)/\rho_w\right]^{5/3} {d_{40}}^{1.5} S^{-7/6} m_2\right\}^{1/(1-n_2)} \tag{21}$$

where $m_1 = 0.2354$, $m_2 = 4.789$, $n_1 = 0.2266$, and $n_2 = 0.1970$ are empirical coefficients associated with the hydraulic radius and width along the flow cross-section. d_m is the mean diameter, which is usually represented by the median grain size d_{50}, and S is the mean bed gradient of the river.

Both the critical shear stress and the critical discharge values for different reference diameters obtained by the formulas mentioned above are summarized in Table 3. When applying the Shields function (Eq. (14)) to sediments, a characteristic grain size (d_{50}) is usually chosen to represent the entire grain size distribution. This equation assumes that all grain sizes have equal mobility when bed shear stress (τ) greatly exceeds the critical shear stress (τ_c). Some empirical thresholds, such as $\tau/\tau_c > 1.4$ (Parker and Klingeman, 1982) and $\tau/\tau_c > 2.0$ (Wilcock, 1992), are recognized as equal mobility conditions. The critical shear stress estimated from Eq. (14) is equal to 104.17 N/m^2 in our study. We chose the mean flow depths $h = 0.45$ m (Dam No. 1) and 0.60 m (Dam No. 2) through visual inspection of the water level gauge installed downstream of the dams. The bed shear stresses ($\tau = \rho_w g h S$, where h denotes mean flow depth) are 231.32 N/m^2 for Dam No. 1 and 308.43 N/m^2 for Dam No. 2, indicating that both cases satisfy the equal mobility condition, which assumes that all particles have an equal chance of being transported downstream. In addition, Montgomery et al. (1999) reported that equal mobility could be attained when the discharge is 2.5 times larger

Table 3
Critical shear stress (τ_c) and critical discharge (Q_c) are obtained by the formulas analyzed in the text (see reference numbers). Values derived from the characteristic diameters different from those used in the original formulas are shown in brackets.

Item	Eq.	d_5	d_{16}	d_{50}	d_{84}	d_{95}
Critical shear stress (N m^{-2})	(14)	(2.52)	(18.48)	104.17	(364.10)	(458.83)
	(16)	4.26	12.79	12.27	21.13	23.91
	(17)	10.4	13.42	16.74	19.65	20.24
	(18)	(3.80e-08)	(2.50e-04)	0.52	(129.19)	(358.48)
Critical discharge (m^3/s)	(19)	(1.66e-05)	(6.87e-04)	1.74e-02	(1.80e-01)	(2.77e-01)
	(20)	(4.41e-05)	1.82e-03	(4.61e-02)	(4.77e-01)	(7.35e-01)
	(21)	(7.08e-05)	(2.93e-03)	(7.40e-02)	(7.66e-01)	(1.18e-00)

than the critical discharge for incipient motion. In our study, the peak discharge (see Fig. 13a) of Dam No. 1 (1.77 m^3/s) and Dam No. 2 (3.38 m^3/s) is 3.4 times and 6.5 times larger than the critical discharge (0.52 m^3/s) calculated by Eq. (18). This suggests all particles will experience equal mobility during the experiments.

Besides the critical shear force on representative particle d_{50}, different critical shear stresses ($\tau_{c,i}$) are used in heterogeneous sediments for each grain size fraction (i). We tested a series of characteristic diameters ranging from fine to coarse grain size fractions using Eqs. (16) and (17), and are shown in Table 3. Generally, the critical shear stresses derived from two equations increase with the increase of the grain size and are an order of magnitude smaller than the calculated Shields number (Eq. (14)). Note that the portion of the coarse particles (e.g., d_{84} and d_{95}) have smaller critical shear stresses than they would have relative to uniform sediments. This is different for the portion of the fine particles (e.g., d_5), which have larger critical shear stresses instead. This can be explained by hiding and exposure effects in non-uniform sediment mixtures: coarser particles are more exposed to the flow while finer particles are hidden between coarser particles (Frings, 2008). Hiding-exposure effects reduce the differences in critical shear stress between the various grain-size fractions, making the entrainment process weakly size-selective than indicated by Shields theory, thereby promoting equal mobility. The bed shear stress (τ) in our study is larger than the $\tau_{c,i}$ for both the fine and coarse grain size fractions, which satisfies the requirement for equal mobility entrainment. The grain size distribution also controls the hiding-exposure effect. Weakly bimodal sediments exhibit pronounced hiding-exposure effects, which in turn cause equal entrainment mobility (Wilcock, 1993; Frings, 2008; Turowski et al., 2009). Recall that the bimodality index $B^* = 1.64$, calculated using Eq. (1), is smaller than the limit value of 1.7 (Wilcock, 1993), indicating that the sediments used in this study are weakly bimodal. Hiding-exposure effects are pronounced, and the sediment entrainment process is less size-selective, which means that the particles in our experiments are equally mobile.

Similarly, a positive correlation is observed between critical discharge and grain size (Table 3). The critical discharges are larger than the original values since reference diameters are larger than those used in the original works. Eqs. (19), (20), and (21) show similar critical discharge for the same reference diameters. It is worth noting that when d_{95} of the coarsest sample is entered into these equations, the largest critical discharge is 1.18 m^3/s, which is less than the peak discharge (see Fig. 13a) for Dam No. 1 (1.77 m^3/s) and Dam No. 2 (3.38 m^3/s). This indicates that less grain-size-selective entrainment in the overall sediment transport process. This study shows that equal mobility likely occurs for very high-magnitude flows like infrequent flood events similar to those in Mao and Lenzi (2007).

Equal entrainment mobility (caused by high shear stress or discharge) enables the transport of all gravel-size fractions in the bed but diminishes the potential for downstream fining. Another potential reason is the unchanged linear bed profile (see Fig. 17a and b). The sediment transport must be equal over the entire domain to keep this equilibrium bed profile. This also indicates that sediment transport in this condition no longer depends on grain size.

In addition, the experimental data illustrates a periodic variation in the particle size (Fig. 17c) and is characterized by a sinusoidal function rather than an exponentially decreasing trend. This variation is probably due to (1) the wide range of grain sizes of materials (Folk and Ward, 1957), (2) the continuous supply of soils from the eroded dams, and (3) the removal of coarser sediments deposited during earlier aggradation phases by the flood. The non-uniform relationship between grain size and distance suggests that simple proximal to distal models may be inappropriate for landslide dam failure sedimentary sequences since 'proximal' and 'distal' conditions may repeatedly occur along the downstream direction.

5. Conclusions

Large-scale field modeling tests are conducted to understand the potential effects of seepage flow on the dam settlement, deformation, overtopping failure processes, and the variation of channel morphology caused by outburst flood. From the analysis of the experimental results, we can conclude that:

(1) Seepage flows can significantly influence the landslide dam stability. The maximum settlement deformation of Dam No. 1 (0.084 m) was only 22% of the maximum settlement deformation of Dam No. 2 (0.379 m). The seepage flow did not reach the downstream dam face before the overtopping occurred in Dam No. 1. However, significant seepage flow is evident at the downstream surface of Dam No. 2, indicating that the failure is induced by the coupling of seepage flow and overtopping water.
(2) Seepage flows accelerate the overtopping failure (two to three times faster) and double the magnitude of outburst discharge. The discharge develops simultaneously with the breach size (e.g., breach area and breach width). The outburst discharge of Dam No. 1 is significantly influenced by the grain size d_{50}, whereas d_{50} has minimal influence on Dam No. 2.
(3) The topography of the downstream channel is controlled by the outburst flood induced by the coupling of the overtopping and seepage flows. If the dam failure is caused by the coupling of seepage and overtopping flows (e.g., Dam No. 2), the channel bed close to the downstream dam toe will be eroded with deposition later. This is different from the processes wherein only overtopping is considered (e.g., Dam No. 1). In such cases, deposition mainly forms downstream. The equal entrainment mobility caused by high shear stress or discharge and the stable linear longitudinal profile decreases the downstream fining by enabling transport for all particles in the channel bed.

Generally, the seepage flows in landslide dams play an essential role in landslide dam failure. The seepage flows result in severe settlement deformation, accelerate the erosion process, and amplify the outburst flood during the overtopping breach. The "overtopping and seepage" failure mode is more dangerous than the overtopping mode.

Author statement

Gordon G. D. Zhou made substantial contributions to the conception, validation, project administration, funding acquisition.

Shuai Li made substantial contributions to the Methodology, Supervision, and Writing -Original draft preparation.

Xueqiang Lu made substantial contributions to the resources, data curation, and investigation.

Hui Tang made substantial contributions to the reviewing and editing.

Declaration of Competing Interest

The authors declare that they have no known competing financial interests or personal relationships that could have appeared to influence the work reported in this paper.

Acknowledgments

The authors acknowledge financial support from the Second Tibetan Plateau Scientific Expedition and Research Program (Grant No. 2019QZKK0902), the National Natural Science Foundation of China (Grant no. 42007270), the Key Research Program of Chinese Academy of Sciences (Grant no. KFZD-SW-425), the Sichuan Science and Technology Program (Grant No. 2019YJ0009), Helmholtz-OCPC Postdoc Program fellowship (ZD2019042), Sino-German Mobility programme (Grant no. M-0145), and the Youth Innovation Promotion Association CAS (2022379). Furthermore, we are grateful to Prof. Wei Wu from the University of Natural Resources and Life Sciences, Vienna for his supply in the Geo-Studio simulations, as well as Dr. Kahlil Fredrick E. Cui and Dr. Pamela Roque for their contributions to polish the English. Finally, we thank the Editor, Associate Editor, and anonymous reviewers for their constructive suggestions that improved the clarity of the manuscript.

References

Alyamani, M.S., Sen, Z., 1993. Determination of hydraulic conductivity from complete grain-size distribution curves. Groundwater. 31 (4), 551–555. https://doi.org/10.1111/j.1745-6584.1993.tb00587.x.

Andrews, E.D., 1983. Entrainment of gravel from naturally sorted riverbed material. Geol. Soc. Am. Bull. 94 (10), 1225–1231. https://doi.org/10.1130/0016-7606(1983)94<1225:EOGFNS>2.0.CO;2.

ASTM, D, 2010. Standard Test Methods for Measurement of Hydraulic Conductivity of Saturated Porous Materials using a Flexible Wall Permeameter. D5084.

Awal, R., Nakagawa, H., Kawaike, K., Baba, Y., Zhang, H., 2008. Experimental study on prediction of failure mode of landslide dams. In: Proceedings 4th International Conference on Scour and Erosion (ICSE-4). November 5–7, 2008, Tokyo, Japan, pp. 655–660.

Bathurst, J.C., Hey, R.D., Thorne, C.R. (Eds.), 1987. Sediment Transport in Gravel-Bed Rivers. Wiley, Chichester, UK, pp. 453–491.

Bonnard, C., 2011. Technical and human aspects of historic rockslide-dammed lakes and landslide dam breaches. In: Natural and Artificial Rockslide Dams. Springer, Berlin, Heidelberg, pp. 101–122. https://doi.org/10.1007/978-3-642-04764-0_3.

Casagli, N., Ermini, L., Rosati, G., 2003. Determining grain size distribution of the material composing landslide dams in the Northern Apennines: sampling and processing methods. Eng. Geol. 69 (1–2), 83–97. https://doi.org/10.1016/S0013-7952(02)00249-1.

Chai, H.J., Liu, H.C., Zhang, Z.Y., Xu, Z.W., 2000. The distribution, causes and effects of damming landslides in China. J. Chengdu Inst. Technol. 27 (3), 302–307.

Chang, D.S., Zhang, L.M., 2013a. Critical hydraulic gradients of internal erosion under complex stress states. J. Geotech. Geoenviron. 139 (9), 1454–1467. https://doi.org/10.1061/(ASCE)GT.1943-5606.0000871.

Chang, D.S., Zhang, L.M., 2013b. Extended internal stability criteria for soils under seepage. Soils Found. 53 (4), 569–583. https://doi.org/10.1016/j.sandf.2013.06.008.

Chanson, H., 2004. Hydraulics of Open Channel Flow. Elsevier.

Chen, S.C., Lin, T.W., Chen, C.Y., 2015. Modeling of natural dam failure modes and downstream riverbed morphological changes with different dam materials in a flume test. Eng. Geol. 188, 148–158. https://doi.org/10.1016/j.enggeo.2015.01.016.

Chen, C., Zhang, L.M., Pei, L., Wu, Z.Y., 2020. Soil deformations induced by particle removal under complex stress states. J. Geotech. Geoenviron. 146 (9), 04020085. https://doi.org/10.1061/(ASCE)GT.1943-5606.0002342.

Cheng, N.S., Chiew, Y.M., 1999. Incipient sediment motion with upward seepage. J. Hydraul. Res. 37 (5), 665–681. https://doi.org/10.1080/00221689909498522.

Coleman, S.E., Andrews, D.P., Webby, M.G., 2002. Overtopping breaching of noncohesive homogeneous embankments. J. Hydraul. Eng. 128 (9), 829–838. https://doi.org/10.1061/(ASCE)0733-9429(2002)128:9(829).

Costa, J.E., Schuster, R.L., 1988. The formation and failure of natural dams. Geol. Soc. Am. Bull. 100 (7), 1054–1068. https://doi.org/10.1130/0016-7606(1988)100<1054:TFAFON>2.3.CO;2.

Cui, P., Chen, X.Q., Zhu, Y.Y., Su, F.H., Wei, F.Q., Han, Y.S., Liu, H.J., Zhuang, J.Q., 2011. The Wenchuan earthquake (May 12, 2008), Sichuan province, China, and resulting geohazards. Nat. Hazards 56 (1), 19–36. https://doi.org/10.1007/s11069-009-9392-1.

Dai, F.C., Lee, C.F., Deng, J.H., Tham, L.G., 2005. The 1786 earthquake-triggered landslide dam and subsequent dam-break flood on the Dadu River, southwestern China. Geomorphology. 65 (3–4), 205–221. https://doi.org/10.1016/j.geomorph.2004.08.011.

Engelund, F., 1965. A criterion for the occurrence of suspended load. La Houille Blanche 8 (7).

Ermini, L., Casagli, N., 2003. Prediction of the behaviour of landslide dams using a geomorphological dimensionless index. Earth Surf. Process. Landforms. 28 (1), 31–47. https://doi.org/10.1002/esp.424.

Fan, X., Scaringi, G., Korup, O., West, A.J., van Westen, C.J., Tanyas, H., Hovirus, N., Hales, T.C., Jibson, R.W., Allstadt, K.E., Zhang, L.M., Evans, S.G., Xu, C., Li, G., Pei, X.J., Xu, Q., Huang, R.Q., 2019. Earthquake-induced chains of geologic hazards: patterns, mechanisms, and impacts. Rev. Geophys. 57 (2), 421–503. https://doi.org/10.1029/2018RG000626.

Federal Energy Regulatory Commission (FERC), 1987. Engineering Guidelines for the Evaluation of Hydropower Projects. FERC 0119–1. Office of Hydropower Licensing, Washington, DC.

Feng, Z.Y., Huang, H.Y., Chen, S.C., 2020. Analysis of the characteristics of seismic and acoustic signals produced by a dam failure and slope erosion test. Landslides. 17 (7), 1605–1618. https://doi.org/10.1007/s10346-020-01390-x.

Ferguson, R.I., 2012. River channel slope, flow resistance, and gravel entrainment thresholds. Water Resour. Res. 48 (5) https://doi.org/10.1029/2011WR010850.

Folk, R.L., Ward, W.C., 1957. Brazos River bar [Texas]; a study in the significance of grain size parameters. J. Sediment. Res. 27 (1), 3–26. https://doi.org/10.1306/74D70646-2B21-11D7-8648000102C1865D.

Fread, D.L., 1988. BREACH, an erosion Model for Earthen Dam Failures. Hydrologic Research Laboratory, National Weather Service, NOAA.

Fredlund, D.G., 2006. Unsaturated soil mechanics in engineering practice. J. Geotech. Geoenviron. 132 (3), 286–321. https://doi.org/10.1061/(ASCE)1090-0241(2006)132:3(286).

Fredlund, D.G., Xing, A., Huang, S., 1994. Predicting the permeability function for unsaturated soils using the soil-water characteristic curve. Can. Geotech. J. 31 (4), 533–546. https://doi.org/10.1139/t94-062.

Frings, R.M., 2008. Downstream fining in large sand-bed rivers. Earth Sci. Rev. 87 (1–2), 39–60. https://doi.org/10.1016/j.earscirev.2007.10.001.

Hakimzadeh, H., Nourani, V., Amini, A.B., 2014. Genetic programming simulation of dam breach hydrograph and peak outflow discharge. J. Hydrol. Eng. 19 (4), 757–768. https://doi.org/10.1061/(ASCE)HE.1943-5584.0000849.

Hanson, G.J., Cook, K.R., Hunt, S.L., 2005. Physical modeling of overtopping erosion and breach formation of cohesive embankments. Transact. ASAE. 48 (5), 1783–1794. https://doi.org/10.13031/2013.20012.

Hazen, A., 1911. Discussion: dams on sand foundations: transactions. In: American Society of Civil Engineers, 73, p. 199.

Indri, E., 1941. II problema del trasporto solido ed i risultati di recenti ricerche. L'Energia Elettrica 19, 91.

Jiang, X., Wei, Y., 2020. Erosion characteristics of outburst floods on channel beds under the conditions of different natural dam downstream slope angles. Landslides. 17 (8), 1823–1834. https://doi.org/10.1007/s10346-020-01381-y.

Johnson, F.A., Illes, P., 1976. A classification of dam failures. Int. Water Power Dam Constr. 28 (12), 43–45.

Korup, O., 2002. Recent research on landslide dams-a literature review with special attention to New Zealand. Prog. Phys. Geogr. 26 (2), 206–235. https://doi.org/10.1191/0309133302pp333ra.

Krumbein, W.C., 1934. Size frequency distributions of sediments. J. Sediment. Res. 4 (2), 65–77. https://doi.org/10.1306/D4268EB9-2B26-11D7-8648000102C1865D.

Liao, W.M., Chou, H.T., 2003. Debris flows generated by seepage failure of landslide dams. In: 3rd International Conference on Debris-flow Hazards Mitigation: Mechanics, Prediction, and Assessment. Rotterdam:[sn], pp. 315–325.

Liu, N., Chen, Z., Zhang, J., Lin, W., Chen, W., Xu, W., 2010. Draining the Tangjiashan barrier lake. J. Hydraul. Eng. 136 (11), 914–923. https://doi.org/10.1061/(ASCE)HY.1943-7900.0000241.

Macchione, F., 2008. Model for predicting floods due to earthen dam breaching. I: Formulation and evaluation. J. Hydraul. Eng. 134 (12), 1688–1696. https://doi.org/10.1061/(ASCE)0733-9429(2008)134:12(1688).

Mao, L., Lenzi, M.A., 2007. Sediment mobility and bedload transport conditions in an alpine stream. Hydrol. Processes: An Int. J. 21 (14), 1882–1891. https://doi.org/10.1002/hyp.6372.

Meyer-Peter, E., Favre, H., Einstein, H.A., 1934. Neuere versuchsresultate über den geschiebetrieb. Schweizerische Bauzeitung. 103 (13), 147–150.

Montgomery, D.R., Panfil, M.S., Hayes, S.K., 1999. Channel-bed mobility response to extreme sediment loading at Mount Pinatubo. Geology. 27 (3), 271–274. https://doi.org/10.1130/0091-7613(1999)027<0271:CBMRTE>2.3.CO;2.

Morrism, 2008. IMPACT Project Field Tests Data Analysis. H R Wallingford, Oxfordshire.

Mu, Q.Y., Dong, H., Liao, H.J., Dang, Y.J., Zhou, C., 2020. Water-retention curves of loess under wetting− drying cycles. Géotechnique Letters. 10 (2), 135–140. https://doi.org/10.1680/jgele.19.00025.

Ng, C.W., Pang, Y.W., 2000. Experimental investigations of the soil-water characteristics of a volcanic soil. Can. Geotech. J. 37 (6), 1252–1264. https://doi.org/10.1139/t00-056.

Okeke, A.C.U., Wang, F., 2016. Critical hydraulic gradients for seepage-induced failure of landslide dams. Geoenviron. Dis. 3 (1), 1–22. https://doi.org/10.1186/s40677-016-0043-z.

Parker, G., Klingeman, P.C., 1982. On why gravel bed streams are paved. Water Resour. Res. 18 (5), 1409–1423. https://doi.org/10.1029/WR018i005p01409.

Peng, M., Zhang, L.M., 2012. Breaching parameters of landslide dams. Landslides. 9 (1), 13–31. https://doi.org/10.1007/s10346-011-0271-y.

Peng, M., Zhang, L.M., 2013. Dynamic decision making for dam-break emergency management–part 2: Application to Tangjiashan landslide dam failure. Nat. Hazards Earth Syst. Sci. 13 (2), 439–454. https://doi.org/10.5194/nhess-13-439-2013.

Peng, M., Zhang, L.M., Chang, D.S., Shi, Z.M., 2014. Engineering risk mitigation measures for the landslide dams induced by the 2008 Wenchuan earthquake. Eng. Geol. 180, 68–84. https://doi.org/10.1016/j.enggeo.2014.03.016.
Peng, M., Zhang, L., Chang, D., Xu, Y., 2016. Dam Failure Mechanisms and Risk Assessment. John Wiley & Sons.
Pickert, G., Weitbrecht, V., Bieberstein, A., 2011. Breaching of overtopped river embankments controlled by apparent cohesion. J. Hydraul. Res. 49 (2), 143–156. https://doi.org/10.1080/00221686.2011.552468.
Richards, L.A., 1931. Capillary conduction of liquids through porous mediums. Physics. 1 (5), 318–333. https://doi.org/10.1063/1.1745010.
Schmocker, L., Hager, W.H., 2012. Plane dike-breach due to overtopping: Effects of sediment, dike height and discharge. J. Hydraul. Res. 50 (6), 576–586. https://doi.org/10.1080/00221686.2012.713034.
Schoklitsch, A., 1962. Handbuch Des Wasserbaues, 3rd edn. Springer, Wien.
Schuster, R.L., Costa, J.E., 1986. Perspective on landslide dams. In Landslide Dams: Processes, risk, and Mitigation. In: Proceedings of a Session in Conjunction with the ASCE Convention, pp. 1–20.
Shang, Y., Yang, Z., Li, L., Liao, Q., Wang, Y., 2003. A super-large landslide in Tibet in 2000: background, occurrence, disaster, and origin. Geomorphology. 54 (3–4), 225–243. https://doi.org/10.1016/S0169-555X(02)00358-6.
Shields, A., 1936. Anwendung der Ahnlichkeitsmechanik Und der Turbulenzforschung Auf Die Geschiebebewegung: Mitteilungen Preubische Versuchsanstalt für Wasserbau Und Schiffbau, p. P26.
Singh, K.P., Snorrason, A., 1984. Sensitivity of outflow peaks and flood stages to the selection of dam breach parameters and simulation models. J. Hydrol. 68 (1–4), 295–310. https://doi.org/10.1016/0022-1694(84)90217-8.
Trieste, D.J., 1988. Downstream Hazard Classification Guidelines. US Department of the Interior, Bureau of Reclamation.
Turowski, J.M., Yager, E.M., Badoux, A., Rickenmann, D., Molnar, P., 2009. The impact of exceptional events on erosion, bedload transport and channel stability in a step-pool channel. Earth Surf. Process. Landf. 34 (12), 1661–1673. https://doi.org/10.1002/esp.1855.
Walder, J.S., 2016. Dimensionless erosion laws for cohesive sediment. J. Hydraul. Eng. 142 (2), 04015047. https://doi.org/10.1061/(ASCE)HY.1943-7900.0001068.
Walder, J.S., O'Connor, J.E., 1997. Methods for predicting peak discharge of floods caused by failure of natural and constructed earthen dams. Water Resour. Res. 33 (10), 2337–2348. https://doi.org/10.1029/97WR01616.
Walder, J.S., Iverson, R.M., Godt, J.W., Logan, M., Solovitz, S.A., 2015. Controls on the breach geometry and flood hydrograph during overtopping of noncohesive earthen dams. Water Resour. Res. 51 (8), 6701–6724. https://doi.org/10.1002/2014WR016620.
Wetmore, J.N., Fread, D.L., 1981. The NWS Simplified Dam-Break Flood Forecasting Model. National Weather Service, Silver Spring, Maryland, pp. 164–197.
White, D.J., Take, W.A., Bolton, M.D., 2003. Soil deformation measurement using particle image velocimetry (PIV) and photogrammetry. Geotechnique. 53 (7), 619–631. https://doi.org/10.1680/geot.2003.53.7.619.
Wilcock, P.R., 1992. Experimental investigation of the effect of mixture properties on transport dynamics. In: Dynamics of Gravel-Bed Rivers, p. 109.
Wilcock, P.R., 1993. Critical shear stress of natural sediments. J. Hydraul. Eng. 119 (4), 491–505. https://doi.org/10.1061/(ASCE)0733-9429(1993)119:4(491).
Xiangang, J., Jiahua, H., Yunwei, W., Zhipan, N., Fenghui, C., Zuyin, Z., Zhanyuan, Z., 2018. The influence of materials on the breaching process of natural dams. Landslides. 15 (2), 243–255. https://doi.org/10.1007/s10346-017-0877-9.
Xu, Y., Zhang, L.M., 2009. Breaching parameters for earth and rockfill dams. J. Geotech. Geoenviron. 135 (12), 1957–1970. https://doi.org/10.1061/(ASCE)GT.1943-5606.0000162.
Xu, Q., Fan, X.M., Huang, R.Q., Westen, C.V., 2009. Landslide dams triggered by the Wenchuan Earthquake, Sichuan Province, south west China. Bull. Eng. Geol. Environ. 68 (3), 373–386. https://doi.org/10.1007/s10064-009-0214-1.
Yan, Y., Cui, Y., Tian, X., Hu, S., Guo, J., Wang, Z., Yin, S.Y., Liao, L., 2020a. Seismic signal recognition and interpretation of the 2019 "7.23" Shuicheng landslide by seismogram stations. Landslides 17, 1191–1206. https://doi.org/10.1007/s10346-020-01358-x.
Yan, Y., Cui, Y., Guo, J., Hu, S., Wang, Z., Yin, S., 2020b. Landslide reconstruction using seismic signal characteristics and numerical simulations: Case study of the 2017 "6.24" Xinmo landslide. Eng. Geol. 270, 105582 https://doi.org/10.1016/j.enggeo.2020.105582.
Yin, Y., Wang, F., Sun, P., 2009. Landslide hazards triggered by the 2008 Wenchuan earthquake, Sichuan, China. Landslides. 6 (2), 139–152. https://doi.org/10.1007/s10346-009-0148-5.
Yolcubal, I., Brusseau, M.L., Artiola, J.F., Wierenga, P.J., Wilson, L.G., 2004. Environmental physical properties and processes. In: Environmental Monitoring and Characterization. Elsevier Inc., pp. 207–239
Zhang, J., Li, Y., Xuan, G., Wang, X., Li, J., 2009. Overtopping breaching of cohesive homogeneous earth dam with different cohesive strength. Sci. China Series E: Technol. Sci. 52 (10), 3024–3029. https://doi.org/10.1007/s11431-009-0275-1.
Zhang, L., Xiao, T., He, J., Chen, C., 2019. Erosion-based analysis of breaching of Baige landslide dams on the Jinsha River, China, in 2018. Landslides. 16 (10), 1965–1979. https://doi.org/10.1007/s10346-019-01247-y.
Zhou, G.G.D., Ng, C.W., 2010. Dimensional analysis of natural debris flows. Can. Geotech. J. 47 (7), 719–729. https://doi.org/10.1139/T09-134.
Zhou, G.G.D., Zhou, M., Shrestha, M.S., Song, D., Choi, C.E., Cui, K.F.E., Peng, M., Shi, Z., Zhu, X., Chen, H., 2019a. Experimental investigation on the longitudinal evolution of landslide dam breaching and outburst floods. Geomorphology. 334, 29–43. https://doi.org/10.1016/j.geomorph.2019.02.035.
Zhou, M.J., Zhou, G.G.D., Cui, K.F.E., Song, D.R., Lu, X.Q., 2019b. Influence of inflow discharge and bed erodibility on outburst flood of landslide dam. J. Mt. Sci. 16 (4), 778–792. https://doi.org/10.1007/s11629-018-5312-8.
Zhu, P.Y., Li, T., 2001. Flash flooding caused by landslide dam failure. In: ICIMOD Newsletter No. 38.
Zhu, X., Peng, J., Jiang, C., Guo, W., 2019. A preliminary study of the failure modes and process of landslide dams due to upstream flow. Water. 11 (6), 1115. https://doi.org/10.3390/w11061115.
Zhu, X., Peng, J., Liu, B., Jiang, C., Guo, J., 2020. Influence of textural properties on the failure mode and process of landslide dams. Eng. Geol. 271, 105613 https://doi.org/10.1016/j.enggeo.2020.105613.